NTNU

Norwegian University of
Science and Technology

Force Field Identification and Positioning Control of an Autonomous Vessel using Inertial Measurement Units

Guttorm Udjus

Marine Technology
Submission date: June 2017
Supervisor: Roger Skjetne, IMT
Co-supervisor: Hans-Martin Heyn, IMT
Dong T. Nguyen, IMT

Norwegian University of Science and Technology
Department of Marine Technology

NTNU Trondheim
Norwegian University of Science and Technology
Department of Marine Technology

MSC THESIS DESCRIPTION SHEET

Name of the candidate: Udjus, Guttorm

Field of study: Marine control engineering

Thesis title (Norwegian): Identifisering av kraftfelt og posisjonsstyring av eit autonomt fartøy ved bruk av inertielle målesensorer

Thesis title (English): Force field identification and positioning control of an autonomous vessel using inertial measurement units

Background

The design of autonomous surface vessels is increasing in speed, and both the academia and maritime industry are doing research on the topic. One important aspect of an autonomous marine vehicle is the situational awareness of the vehicle by increased perception of environmental loads such as wind, waves, and current. Autonomous systems require novel sensor systems that replace or even exceed the capabilities of a human operator, which is of high importance regarding safety and performance in autonomous operations.

There are several approaches that can be used to increase the awareness of the loading situation for the vehicle. A bio-inspired solution is how a fish sense flow and navigate in a current. The fish has a lateral-line sensing organ, which enables it to detect changes in pressure and thus swim graciously in the flow of ocean or river currents. For a marine vehicle, the understanding of surrounding environment can be done through different types of sensors. An array of inertial measurement units mounted along the vessel hull provides detailed information about the forces acting on the vessel. These will measure local accelerations which, if the vessel is rigid, can be fused to a global acceleration vector. If not rigid, the local accelerations will give information on how the external forces distribute spatially and temporally along the ship structure. This may enable greater situational awareness, and the objective for this thesis is to set up and utilize such a system to obtain better control and decision support of the vessel in autonomous operations.

Scope of Work

1) Perform a background and literature review to provide information and relevant references on:
   a) Autonomy layers and aspects related to increased perception of environmental loads for an autonomous vessel:
      - Use of IMUs and methods for analyzing acceleration data.
      - Distribution of loads acting on flexible surface vessels.
      - Loads from waves and sea-ice.
   b) Methods for vaning vessels in a force field.
   c) Relevant IMU sensors and their properties.

   Write a list with abbreviations and definitions of terms, explaining relevant concepts related to the literature study and project assignment.

2) Implement and test an experimental setup for C/S Inocean Cat I Drillship in MC-Lab, giving spatially distributed and time synchronized acceleration measurements along the hull. Test in waves of varying incoming directions and collect data.

3) Perform statistical analysis (correlation analysis; probability distribution fit; extreme load analysis; etc.) of the data and discuss the spatial variability of the acceleration data along the hull side.

4) Propose a method to identify the magnitude and direction of the local forces acting on the hull in real time or online. Can you visualize the force field to show how it acts on the vessel with time, e.g. by a good visual plot and animations with time?

5) Propose a guidance function that based on the distributed force field calculates an optimal heading of the vessel, as input to heading control.

Tentatively:

6) Implement the optimal heading guidance function for real-time control, and interface this to the DP control system for C/S Inocean Cat I Drillship. Test in MC-Lab with different initial headings relative to the waves.

Specifications

The scope of work may prove to be larger than initially anticipated. By the approval from the supervisor, described topics may be deleted or reduced in extent without consequences with regard to grading.

The candidate shall present personal contribution to the resolution of problems within the scope of work. Theories and conclusions should be based on mathematical derivations and logic reasoning identifying the various steps in the deduction.

The report shall be organized in a logical structure to give a clear exposition of background, results, assessments, and conclusions. The text should be brief and to the point, with a clear language. Rigorous mathematical deductions and illustrating figures are preferred over lengthy textual descriptions. The report shall have font size 11 pts. It shall be written in English (preferably US) and contain the following elements: Title page, abstract, acknowledgements, thesis specification, list of symbols and acronyms, table of contents, introduction with objective, background, and scope and delimitations, main body with problem formulations, derivations/developments and results, conclusions with recommendations for further work, references, and optional appendices. All figures, tables, and equations shall be numerated. The original contribution of the candidate and material taken from other sources shall be clearly identified. Work from other sources shall be properly acknowledged using quotations and a Harvard citation style (e.g. *natbib* Latex package). The work is expected to be conducted in an honest and ethical manner, without any sort of plagiarism and misconduct. Such practice is taken very seriously by the university and will have consequences. NTNU can use the results freely in research and teaching by proper referencing, unless otherwise agreed upon.

The thesis shall be submitted with a printed and electronic copy to the main supervisor, with the printed copy signed by the candidate. The final revised version of this thesis description must be included. The report must be submitted according to NTNU procedures. Computer code, pictures, videos, data series, and a PDF version of the report shall be included electronically with all submitted versions.

Start date: 15 january, 2017 **Due date:** As specified by the administration.

Supervisor: Roger Skjetne
Co-advisor(s): Hans-Martin Heyn (experimental setup), Dong T. Nguyen (reading draft report, etc.).

Trondheim,

_____

Roger Skjetne
Supervisor

Preface

This master thesis concludes my Master's Degree in Marine Engineering at the Norwegian University of Science and Technology(NTNU), written during spring 2017. The work is to some extent based on the Project thesis carried out fall 2016, however the topic was altered in the beginning of 2017 after discussion with my supervisor Professor Roger Skjetne. The experiments are performed in the Marine Cybernetics Laboratory at NTNU, which was my first experience with the laboratory. Working with hardware and embedded system has been highly educational, and I am grateful for finally experiencing the distinction between computer simulations and real-world applications. This has been very challenging and rewarding, as the scope of work required new knowledge from special fields like electronic engineering and IT. It was also very time-consuming, and more than half of the work on the thesis was spent on hardware preparations.

The thesis provides information on the design of embedded systems consisting of inertial measurement units, for measuring spatially distributed accelerations. Relevant theory for solving the motion estimation problem is presented, together with some proposed methods for estimating direction of incoming waves for a marine surface vessel based on the surrounding force field.

Trondheim, 2017-06-18

Guttorm Udjus

Acknowledgment

I have received much help throughout the work with my thesis, and there are several persons I would like to thank. First, I would like to thank my supervisor Professor Roger Skjetne for pitching me the idea for my thesis. I am also grateful for his guidance whenever I asked for it, and facilitating for my work. In addition, I would like to thank him for providing two co-advisors, Hans-Martin Heyn and Dong Trong Nguyen.

Hans-Martin helped me greatly in my encounter with embedded systems and inertial measurement units, and for that I am thankful. He also guided me in the experiments, and problems related to motion estimation. I would like to thank Dong for helping me on the thesis writing, and input on several of the topics discussed.

In the laboratory I also received help from Jon Bjørnø, Torgeir Wahl and Frode Gran, and without their help the hardware related work would have been much more time-consuming. My co-student, Mads Sig Skinderhaug has also been of great help with issues related to microcontrollers, and for that I am thankful.

Finally, I want to thank my family, both at home in Grimstad and in the student association Mannhullet, for their support and motivation throughout these five years of studies. And a special thank you to my fellow students in Class of 2017, for all the good memories we share.

G.U.

Summary

In this thesis, a system of four sensors for measuring tri-axis translational accelerations and rotational velocities is designed. The sensors were mounted with a spatial distribution on board the ship model C/S Arctic Drillship. Experiments were carried out in the Marine Cybernetics Laboratory at the Norwegian University of Science and Technology, and sensor data was collected for waves with various periods and incoming directions.

The distributed acceleration measurements were used to estimate translational and rotational accelerations in Center of control. By comparing the estimates with the high-accuracy measurements from Qualisys, it was found that the system provides good estimates of the accelerations in Center of control. In addition, the local tri-axis translational accelerations in each sensor frame was estimated, to detect spatial variability of accelerations. This method also performs well, and provides a representation of local forces in the hull.

Three methods to estimate the direction of incoming waves are proposed, where one is based on correlation between motion in roll, pitch and yaw, and the two others are based on local accelerations inside the hull. Analysis of motion in roll, pitch and yaw gave some results. Analysis of the horizontal accelerations in the hull was not successful as to detect the surrounding force field, while the heave accelerations gave a better image of the surrounding waves and forces. An algorithm for online estimation of direction of incoming waves was proposed, which was able to predict the direction of incoming waves for some periods.

For a short video of some of the experiments and findings, the reader is referred to Udjus (2017). In this video, the spatially distributed accelerations in each sensor are shown when the waves hit the vessel.

Sammendrag

I denne avhandlingen er det utviklet et system bestående av fire sensorer for måling av lineære akselerasjoner og rotasjonshastigheter i tre akser. Sensorene ble montert på ulike posisjoner ombord på skipsmodellen C/S Arctic Drillship. Eksperimenter ble utført i Marine Cybernetics laboratoriet på Norges teknisk-naturvitenskapelige universitet, og sensordata ble målt for bølger med ulike perioder og innkommende retninger.

Akselerasjonsmålingene fra de ulike sensorene ble brukt til å estimere lineære- og rotasjonsakselerasjoner i et punkt i skipet, kontrollpunktet. Dette ble sammenlignet med nøyaktige målinger fra Qualisys, som bekreftet at sensorsystemet gir gode estimater av akselerasjonene i kontrollpunktet. I tillegg ble de lokale lineære akselerasjonene i hver sensor estimert for å detektere akselerasjonsfordelingen mellom dem. Denne metoden ga også gode resultater, og gir et bilde av de lokale kreftene innad i skroget.

Tre metoder for å estimere retning til innkommende bølger er forslått, hvorav en er basert på korrelasjon mellom bevegelse i rull, stamp og gir, og de to andre er basert på lokale akselerasjoner i skroget. Noen resultater ble funnet fra analyse av bevegelse i rull, stamp og gir. Analyse av de horisontale kreftene i skroget var ikke vellykket med tanke på estimering av retning til innkommende bølger, mens akselerasjonene i hiv ga et bedre bilde av bølgene og kreftene som virker på skipet. En metode for sanntids beregning av retningen til innkommende bølger ble foreslått, som er i stand til å forutsi retningen til bølgene for noen bølgeperioder.

For en kort video av noen av forsøkene og resultatene, kan leseren se Udjus (2017). Videoen viser de lineære akselerasjonene i hver sensor når bølgene treffer skipsmodellen.

Contents

List of Figures

List of Tables

Nomenclature

Abbreviations

CG	Center of Gravity
CO	Center of Control
DP	Dynamic Positioning
GNC	Guidance, Navigation, Control
I/O	Input/Output
LQG	Linear Quadratic Gaussian
MCLab	Marine Cybernetics Laboratory
PPS	Pulse-Per-Second
PSD	Power Spectral Density
RAO	Response Amplitude Operator
SO	Sensor frame Origin
SPI	Serial Peripheral Interface
SPS	Samples Per Second
TAPM	Thruster-Assisted Position Mooring
TCP	Transmission Control Protocol
UDP	User Datagram Protocol
ZOH	Zero-Order Hold

Terms and concepts

- **Autonomy** is the capability of operating without operator input for extended periods of time. Soerensen (2013) divide autonomy into four levels:
  - **Automatic operation** means the system operates automatically, with high-level human mission planning.
  - **Management by consent** means that the system interprets the situation, and prompts the human operator at important points in time for support.
  - **Semi-autonomous** means that the system makes decisions on its own when human response takes too long.
  - **Highly autonomous** means that the system can operate on its own, and is able to re-plan the mission in case of disturbances.
- **Computer network** is a network of computers that allows for sharing data between them.
- **Dynamic positioning** is the concept of using computer-controlled actuation to maintain a desired position and heading of the vessel.
- **Embedded system** is a computer system that is pre-programmed to do specific tasks, usually in real-time operations.
- **Inertial measurements** are forces measured from an objects resistance to change its current state of motion.
- **Inertial Navigation System** is a system that based on inertial measurements can estimate current velocity and position, used for navigation purposes.
- **Weather vaning** is the concept of aligning the vessel towards the environmental forces to minimize energy consumption in operation.

Chapter 1

Introduction

> Awareness is the first step to action. They have to know something is going on to know to do something about it.
>
> *Derick Virgil*

1.1 Background and motivation

The society is continuously striving to make life easier for men, with an increased speed in the last years. And as technology advances, it finds new range of application. The first self-driven taxi was made available in San Fransisco in 2016. In that very same year, the first package delivery with an autonomous drone was carried out by Amazon in the United Kingdom. As for the shipping industry, automation has been an area of research for more than a century. The first application of automated ship operation was made possible with the development of the gyroscope. Based on the measured heading from the gyroscope, an automatic pilot could steer the heading of the ship without constant human intervention. The first autopilot was dated back to 1911, when Elmer A. Sperry designed the *Metal Mike* (Fossen, 2000). The next revolution within ship automation came with the development of the Kalman filter(Kalman, 1960) and the linear quadratic optimal controllers. The first DP-system based on LQG

controllers was developed by Balchen et al. (1976), which proved to have significant impact on ship operations. In the later years, much research has been put into further automation of marine vessel, both on and under the water surface. Many of the problems addressed are related to maneuvering of marine vehicles, such as path-following and coordinated navigation, see Fossen (2011), Skjetne (2005), Breivik (2010) to mention some. What becomes clear is that the recent research is more concentrated on unmanned operations, with reduced or no human interaction.

From a historical perspective, the maritime industry can be considered as a conservative industry with little enthusiasm to embrace new technology. However, with the current market situation, low income for ship owners and increased focus on environmental emissions, the willingness to look into cost saving technology seems to increase. Fully autonomous operations have a huge potential for cost savings, if successfully implemented. The equipment and system developers for the maritime industry are, like the academia, working on the problems related to autonomous operations. Already next year, the World's first autonomous cargo vessel, YARA Birkeland, is planned to sail in the Norwegian fjords, and is scheduled for fully autonomous operation in 2020 (Kongsberg Maritime, 2017). This will be a giant step for maritime traffic, and sets the start for unmanned marine vehicles. Nevertheless, there are still challenges related to these operations, and this thesis aims to contribute in solving one of the problems, as described in the latter.

One aspect of removing the human operator from the vehicle, is how the vehicle senses its surrounding environment. The forces acting on a marine surface vessel can be divided into four groups, namely waves ,wind, current and ice loads. Estimation of wind forces can be done via measured wind speed and direction. Several methods have been proposed for measuring ocean current, e.g. use of shipborne high-frequency radars as discussed in Gurgel and Essen (2000). As for measuring the wave state, Waals et al. (2002) explored the possibility of using wave height sensors distributed along the hull. Other methods proposed are based on correlation between the ship motion and external forces, by investigating the response amplitude operator

for different directions of incoming waves, as discussed in Tannuri et al. (2003). The force related to ice loads is a much researched topic in recent years, as the maritime society continuous to explore rougher environments. Leira et al. (2009) explored how ice-loads could be estimated with use of spatially distributed strain sensors to measure local stress in the bow.

Seeking motivation in the nature in order to solve complex engineering task has been done for decades. There has been several attempts to optimize ship propulsion inspired from how a fish swims, and ROVs based on eel motion have been developed. One interesting phenomena on the situational awareness topic, is how a fish navigates. It is found that fish have a sensor organ for detecting fluid characteristics, called the lateral line. This organ is composed of sensory units called neuromasts distributed over the body, which provide fish with flow-related information. In Chambers et al. (2014) and Wang et al. (2015), to mention some, an artificial later line system of pressure sensors was used to detect flow features around an underwater vehicle. From Bernoulli's equation it is known that pressure is related to energy. Hence, one can view the lateral line principle as a method of sensing energy distribution around the object. As described in Faltinsen (1993), there is a direct connection between incoming waves and the acceleration of a floating marine vehicle. Thus, another approach to the lateral line sensing can be to measure local accelerations in the object, to determine how the surrounding pressure and forces act on the body. This sums up the motivation for the thesis, and the objective of the thesis is described in the latter.

1.2 Objective and scopes

Measuring local accelerations distributed in the ship hull can be done with accelerometers, or inertial measurement units. Hence, one objective of this thesis is to create a system of inertial measurement units for measuring real-time accelerations spatially distributed inside the hull. By analyzing these acceleration measurements, the force field surrounding the hull should be investigated with the objective of providing information on the environmental forces acting on the body. Based on an increased

situational awareness for the ship, a method for optimal heading should be proposed in order to minimize forces, i.e. a method for weather vaning the ship. In short, the scopes of this thesis are:

- Design and assemble a system of inertial measurement units for time-synchronized measurements of spatially distributed accelerations.
- Perform experiments with C/S Arctic Drillship and collect local accelerations in the hull for different directions of incoming waves.
- Analyze the data with objective of determining how the force field influence the hull.
- Propose a method to identify the direction of incoming waves, and based on this propose a control law for weather optimal heading of a ship.

1.3 Assumptions and limitations

In wave theory it is common to separate between deep and shallow water, as the waves have different behavior. In Pettersen (2007) a rule of thumb is that the assumption of deep water is valid if the average depth is more than half the wave length, which is considered valid in this thesis.

1.4 Organization of thesis

The thesis is organized in seven chapters, where Chapter 1 gives a brief introduction to the problem, and outlines the objective of the thesis. In Chapter 2 the main theory used to solve the problem is described, while Chapter 3 describes the methods for solving the objective. Chapter 4 treats the experimental setup with a description of hardware and software. The experimental results are presented in Chapter 5, while the findings are discussed in Chapter 6. Finally, concluding remarks and suggestions for further work are presented in Chapter 7.

Chapter 2

Modeling and methods

2.1 Kinematics

The theory of kinematics regards the dynamic motion of bodies from a geometrical aspect, and in contradiction to kinetics it does not describe the forces causing the motions. Kinematics is the basis of GNC , as it describes the position and orientation of an object in a coordinate system, or reference frame. For a marine vessel, which has both translational and rotational motions in three axes, six variables are used to describe its position and orientation. Using the definition of Fossen (2011), the 6 DOFs are *surge, sway, heave, roll, pitch* and *yaw*, with positive directions as illustrated in Figure 2.1. This definition is used throughout the thesis to describe the vessel motion.

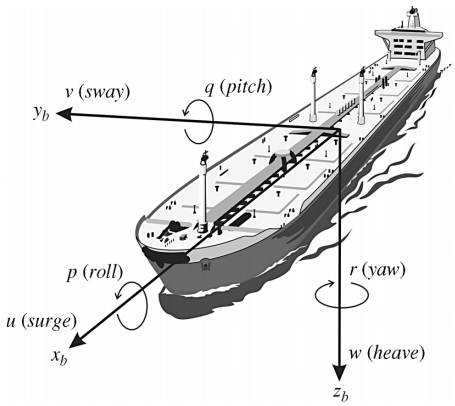

Figure 2.1: Definition of the 6 DOFs. Courtesy of Fossen (2011)

2.1.1 Reference frames

The motion of a body must be described with reference to a coordinate system, and several different reference frames are defined in the literature dependent on the application. The relevant reference frames for this thesis are presented in this section. The connection between the different frames are presented in Figure 2.2a.

- **Earth-Centered Inertial**(ECI), $\{i\} \equiv (o_i, \vec{i}_1, \vec{i}_2, \vec{i}_3)$ defined with origin in the center of the Earth. The x-axis points towards the vernal equinox, and z-axis pointing along the Earth's center of rotation. Finally, the y-axis completes the right-hand rule. This frame can be approximated as an inertial frame for terrestrial navigation, as Newton's laws of motion applies here. Inertial sensor measurements are relative to this frame, and resolved in the sensor frame.

- **Earth-Centered Earth-Fixed**(ECEF), $\{e\} \equiv (o_e, \vec{e}_1, \vec{e}_2, \vec{e}_3)$ has its origin and z-axis coinciding with ECI. The x-axis is pointing towards 0° latitude and 0° longitude, and the y-axis according to the right-hand rule. This frame rotates relative ECI with an angular velocity ω_e, thus it is not an inertial frame. GPS position is given in this frame.

- **North-East-Down**(NED), $\{n\} \equiv (o_n, \vec{n}_1, \vec{n}_2, \vec{n}_3)$ is defined as a coordinate system that is fixed on the Earth, and thus rotates with the Earth. However, as the velocity of a marine vessel usually is small, it can be approximated as an inertial coordinate system. The orientation is such that the first axis points to North, second axis to East and the third axis according to the right-hand rule pointing towards the center of Earth.

- **Basin**, $\{f\} \equiv (o_f, \vec{f}_1, \vec{f}_2, \vec{f}_3)$ is defined as a frame fixed to the basin, with x-axis pointing toward wave-generator, z-axis downwards and y-axis according to the right-hand rule. This coordinate system is generated by the Qualisys Oqus measurement system, such that all position and orientation measurements are relative this coordinate system. For navigation within the basin, this is approximated as an inertial frame.

- **Body**, $\{b\} \equiv (o_b, \vec{b}_1, \vec{b}_2, \vec{b}_3)$ is a coordinate system that is fixed to some point on the vehicle. The first axis points in the longitudinal direction of the vehicle with positive direction towards the bow, the second axis points in the transversal direction of the vehicle with positive direction towards starboard. The third axis is according to the right-hand rule. The origin of this frame is referred to as CO, which is a center of control for the vehicle. This point is usually placed midships in the design waterline, but for convenience it can be chosen to coincide with CG of the model boat.

- **Sensor**, $\{s\} \equiv (o_s, \vec{s}_1, \vec{s}_2, \vec{s}_3)$ is the local coordinate system in each sensor. From the manufacturer, the frame for translational accelerations is oriented according to the left-hand rule, while for rotations the orientation is according to the right-hand screw rule. The translational accelerations from the sensor are multiplied with -1 such that the sensor frame is oriented according to the right-hand rule. The sensor frame from the manufacturer is illustrated in Figure 2.3, with positive directions described by arrows.

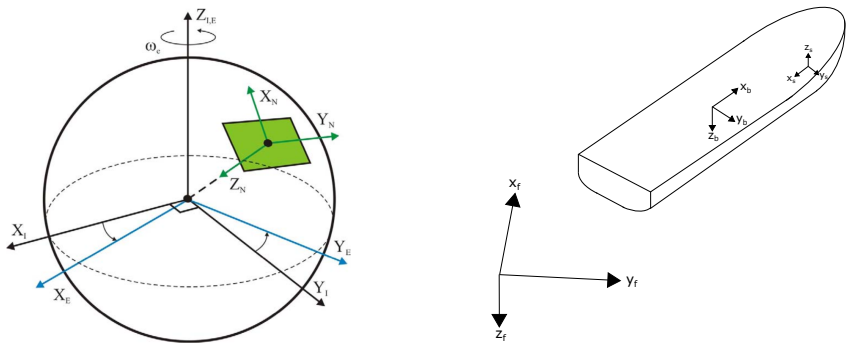

(a) ECI, ECEF and NED frames. Courtesy of Breivik (2010)

(b) Basin, Body and Sensor frames.

Figure 2.2: Illustration of relationship between different reference frames.

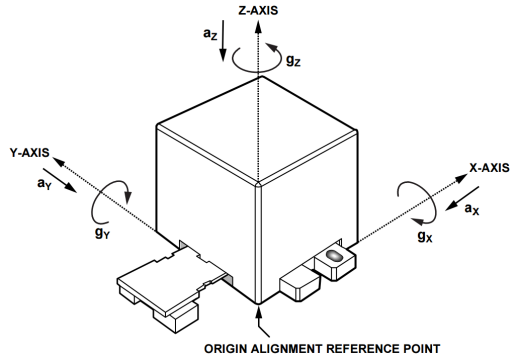

Figure 2.3: Original sensor frame from manufacturer. Courtesy of Analog Devices (2017)

2.1.2 Vectorial notation

The notation used in this thesis is based on the convention defined in Fossen (2011), which is an efficient way of describing the relationship between different frames using sub- and superscripts. In the latter, an explanation of the meaning is described.

$\mathbf{p}^f_{b/f}$ = position of o_b with respect to {f} expressed in {f}

$\mathbf{v}^b_{f/b}$ = linear velocity of the point o_f with respect to {b} expressed in {b}

$\boldsymbol{\omega}^b_{b/f}$ = angular velocity of {b} with respect to {f} expressed in {b}

$\boldsymbol{\Theta}_{fb}$ = Euler angles between {f} and {b}

Now, the position and orientation of the vessel expressed in {f} are given as

$$\mathbf{p}^f_{b/f} = \begin{bmatrix} \mathrm{x} \\ \mathrm{y} \\ \mathrm{z} \end{bmatrix} \qquad \boldsymbol{\Theta}_{fb} = \begin{bmatrix} \phi \\ \theta \\ \psi \end{bmatrix}$$

For the translational and rotational velocities and accelerations expressed in {b} relative {f}, they are defined as

$$\mathbf{v}^b_{b/f} = \begin{bmatrix} \text{u} \\ \text{v} \\ \text{w} \end{bmatrix} \qquad \mathbf{a}^b_{b/f} = \begin{bmatrix} a_x \\ a_y \\ a_z \end{bmatrix} \qquad \boldsymbol{\omega}^b_{b/f} = \begin{bmatrix} \text{p} \\ \text{q} \\ \text{r} \end{bmatrix} \qquad \boldsymbol{\alpha}^b_{b/f} = \begin{bmatrix} \alpha_x \\ \alpha_y \\ \alpha_z \end{bmatrix}$$

2.1.3 Transformations

Based on the vectorial representations presented above, the kinematic equations relating the different frames are given in terms of transformations between them. For linear velocities, the rotation matrix from {b} to {f} according to the *zyx*-convention is:

$$\dot{\mathbf{p}}^f_{b/f} = \mathbf{R}^f_b(\boldsymbol{\Theta}_{fb})\mathbf{v}^b_{b/f} = \begin{bmatrix} c\psi c\theta & -s\psi c\phi + c\psi s\theta s\phi & s\psi s\phi + c\psi c\phi s\theta \\ s\psi c\theta & c\psi c\phi + s\phi s\theta s\psi & -c\psi s\phi + s\theta s\psi c\phi \\ -s\theta & c\theta s\phi & c\theta c\phi \end{bmatrix} \mathbf{v}^b_{b/f} \tag{2.2}$$

where $s\cdot = sin(\cdot)$ and $c\cdot = cos(\cdot)$. This rotation matrix has the property that $\mathbf{R}^f_b(\boldsymbol{\Theta})^{-1} = \mathbf{R}^f_b(\boldsymbol{\Theta})^T = \mathbf{R}^b_f(\boldsymbol{\Theta})$, which is the rotation matrix from {f} to {b}. Transformations of rotational velocities from {b} to {f} are given by the following matrix:

$$\dot{\boldsymbol{\Theta}}_{fb} = \mathbf{T}_\Theta(\boldsymbol{\Theta}_{fb})\boldsymbol{\omega}^b_{b/f} = \begin{bmatrix} 1 & s\phi t\theta & c\phi t\theta \\ 0 & c\phi & -s\phi \\ 0 & s\phi/c\theta & c\phi/c\theta \end{bmatrix} \boldsymbol{\omega}^b_{b/f} \tag{2.3}$$

where $s\cdot = sin(\cdot)$, $c\cdot = cos(\cdot)$ and $t\cdot = tan(\cdot)$. It should be noted that this transformation has a singularity at $\theta = \pm 90°$, but this does not affect surface vehicles. In addition it does not have the same property like the rotation matrix with regard to the inverse, i.e. $\mathbf{T}_\Theta(\boldsymbol{\Theta})^{-1} \neq \mathbf{T}_\Theta(\boldsymbol{\Theta})^T$.

2.1.4 Kinematic equations of motion

6 DOF kinematic equation

The 6 DOF kinematic equation transforming translational and rotational velocities from {b} to {f} is

$$\begin{bmatrix} \dot{\mathbf{p}}^f_{b/f} \\ \dot{\boldsymbol{\Theta}}_{fb} \end{bmatrix} = \begin{bmatrix} \mathbf{R}^f_b(\boldsymbol{\Theta}_{fb}) & \mathbf{0}_{3\times3} \\ \mathbf{0}_{3\times3} & \mathbf{T}_\Theta(\boldsymbol{\Theta}_{fb}) \end{bmatrix} \begin{bmatrix} \mathbf{v}^b_{b/f} \\ \boldsymbol{\omega}^b_{b/f} \end{bmatrix} \tag{2.4}$$

where $\mathbf{0}_{3\times3}$ is a 3 by 3 matrix of zeros. This equation may be written more concise:

$$\dot{\boldsymbol{\eta}} = \mathbf{J}_\Theta(\boldsymbol{\eta})\boldsymbol{\nu} \tag{2.5}$$

where $\boldsymbol{\eta} = \left[\mathbf{p}^f_{b/f}\,;\,\boldsymbol{\Theta}_{fb}\right]$ and $\boldsymbol{\nu} = \left[\mathbf{v}^b_{b/f}\,;\,\boldsymbol{\omega}^b_{b/f}\right]$.

3 DOF kinematic model for translational motion

A 3 DOF kinematic model of the translational motion of the vehicle expressed in {b} may also be derived, by transforming the position measured in {f} to {b}. In the presence of angular velocity of {b}, i.e. $\boldsymbol{\omega}^b_{b/f}$, the position of o_f with respect to {b} expressed in {b} will change due to the rotation. This is accounted for using the vectorial cross product. Consider the following difference equations:

$$\dot{\mathbf{p}}^b_{f/b} = -\mathbf{S}(\boldsymbol{\omega}^b_{b/f})\mathbf{p}^b_{f/b} - \mathbf{v}^b_{b/f} \tag{2.6a}$$

$$\dot{\mathbf{v}}^b_{f/b} = -\mathbf{S}(\boldsymbol{\omega}^b_{b/f})\mathbf{v}^b_{f/b} - \mathbf{a}^b_{b/f} \tag{2.6b}$$

where $\mathbf{p}^b_{f/b} = \mathbf{R}^b_f(\boldsymbol{\Theta}_{fb})\mathbf{p}^f_{f/b}$ and $\mathbf{p}^f_{f/b} = -\mathbf{p}^f_{b/f}$. This corresponds to translating the origin of {f} until it coincides with the origin of {b}, and then rotating according to the *zyx* convention. Further, $\mathbf{S}(\boldsymbol{\omega}^b_{b/f})$ is the skew-symmetric cross product operator defined such that

$$\boldsymbol{\omega}^b_{b/f} \times \mathbf{p}^b_{b/f} = \mathbf{S}(\boldsymbol{\omega}^b_{b/f})\mathbf{p}^b_{b/f} = \begin{bmatrix} 0 & -r & q \\ r & 0 & -p \\ -q & p & 0 \end{bmatrix} \mathbf{p}^b_{b/f} \tag{2.7}$$

2.2 Discrete time

Working with computer processors implies working in discrete time, due to the nature of the processor. However, the real process is a continuous time process, and thus some approximations must be done to make the computer work together with the real process. Measurement of the continuous time process states are done with sensors that sample the current state at time t, with a sampling period T. Lets assume this state works as an input $u(t)$ to a linear continuous-time state-space model:

$$\dot{x}(t) = A(t)x(t) + B(t)u(t) \tag{2.8}$$

Introducing discrete time notation, such that $t_k = kT$ for $k = \{0,1,2,..\}$ and $x(k) = x(kT)$, $x(k+1) = x((k+1)T)$. Assume that the system matrices are constant over the sampling period such that the system is LTI. Further, let us assume that the input signal is piecewise constant over the sampling interval T, which is achieved using the ZOH method. For staircase inputs, this method provides an exact match between the continuous- and discrete-time systems. Now we have that $u(t)$ is constant for $kT \leq t < (k+1)T$, i.e. equal to $u(k)$, and $A(t) = A$,$B(t) = B$. The solution to (2.8) is

$$x(k+1) = e^{AT}x(k) + \int_{kT}^{(k+1)T} e^{A[(k+1)T-\tau]}Bu(k)d\tau \tag{2.9}$$

After integration, this gives the discrete time system

$$x(k+1) = \Phi x(k) + \Delta u(k) \tag{2.10}$$

where

$$\Phi = e^{AT}, \qquad \Delta = A^{-1}(\Phi - I)B \tag{2.11}$$

Discretizing an LTI state-space model in MATLAB using ZOH can be done with the built-in function *c2d(A, B, T)*, which outputs the discrete time system matrices. The function utilize the matrix exponential function *expm.m* to calculate the discrete sys-

tem matrices:

$$\begin{bmatrix} \Phi & \Delta \\ 0 & 1 \end{bmatrix} = expm\left(\begin{matrix} A & B \\ 0 & 0 \end{matrix} \right) T \tag{2.12}$$

For more information on the process of discretization, the reader is referred to Smith (1977).

2.3 Signal processing

Measuring some states in the real world with a sensor will never be a perfect measurement, i.e. the sensor will never output the true state. There might be many error effects on a sensor signal, and there exist several methods for processing the signal output to filter out some of the effects. In Soerensen (2013) methods for testing signals are presented, such as signal range, variance and wild point testing are presented. The objective of these tests are to verify the quality of a signal, and handle it accordingly by for example voting, weighting or rejecting the signal. Wild point testing is done in order to determine whether a signal has been corrupted such that it gives a too high change in the state compared to previous measurements. There are several methods for this test, and a simple model for wild point detection is based on the estimated mean value of the signal plus some window of acceptance based on the variance of the signal. An acceptable sample may be described as:

$$x(k) \in [\bar{x}(k) - a\sigma, \bar{x}(k) + a\sigma] \tag{2.13}$$

where σ is the variance of the signal and a is some tolerance factor.

2.3.1 Filtering

The measurement noise of the signal may be filtered out using some filter. The characteristics of measurement noise is that the frequency of the noise is equal the sampling frequency. This frequency is usually much higher than the process frequency, and thus it is possible to filter out the high-frequency part of the signal. A low-pass filter is

a good method for filtering out the measurement noise. A low-pass filter is based on the following transfer function:

$$\frac{y(s)}{u(s)} = \frac{\omega_c}{\omega_c + s} \tag{2.14}$$

where $\omega_c = 2\pi f_c$ is the cutoff frequency. This is the simplest lowpass filter, and the magnitude response of the filter with $f_c = 10$Hz is illustrated in Figure 2.4. It is clear that the filter has a slowly decreasing response, and it is often desirable to set the curvature of the magnitude response. There are numerous different methods of designing filters, and in this thesis the lowpass equiripple FIR filter using the Parks-McClennan algorithm is chosen. The algorithm is described in Parks and McClellan (1972). The filter characteristic is that it minimizes the maximum ripple over all bands according to Mathworks (2017a), with the possibility of specifying passband and stopband frequency and attenuation. The magnitude response of the filter is illustrated in Figure 2.4, with passband frequency equal 9 Hz, stopband frequency equal 11 Hz, passband attenuation set to 0.5 dB and stopband attenuation set to 10 dB. The performance of both filters are compared for a sinusoidal signal with white noise, see Figure 2.5. It should be noted that the time delay has been corrected for. It is seen from the figure that both filters does a good job removing measurement noise, but the simple filter does not well represent the peaks in the signal.

2.4 Kalman Filter

The Kalman Filter is an algorithm used in a wide variety of applications, and has proven to be very useful in GNC. The algorithm was first presented in Kalman (1960) as a recursive solution for discrete-data linear filtering. Since then, the algorithm has been subject to extensive research and an abundant amount of versions have been developed. In the latter, two versions are presented, namely the discrete time Kalman Filter and an Adaptive Fading Kalman Filter.

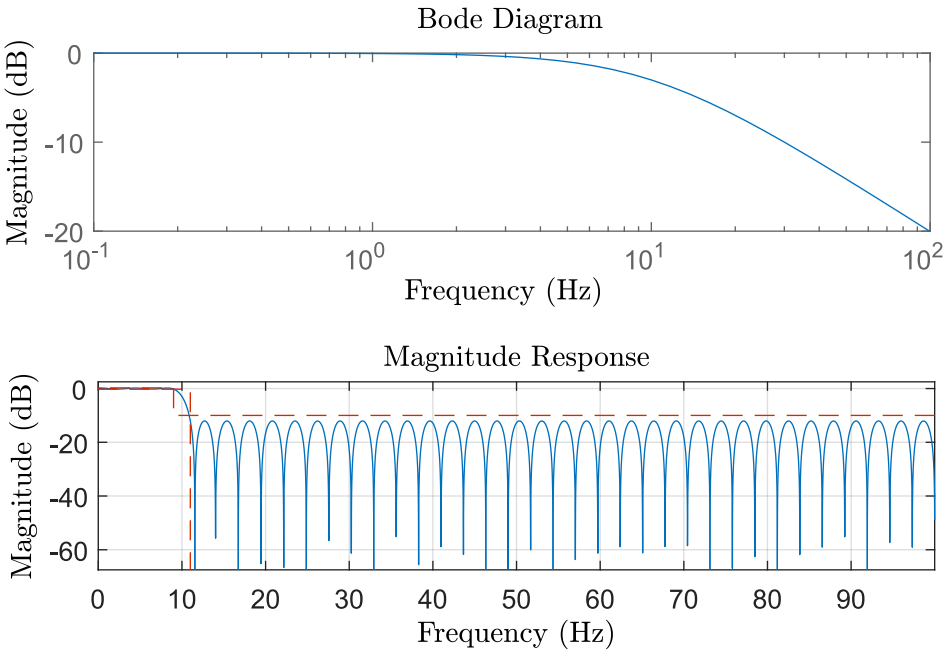

Figure 2.4: Magnitude response for filters. Upper figure illustrates simple low pass filter, and lower figure show the equiripple FIR filter

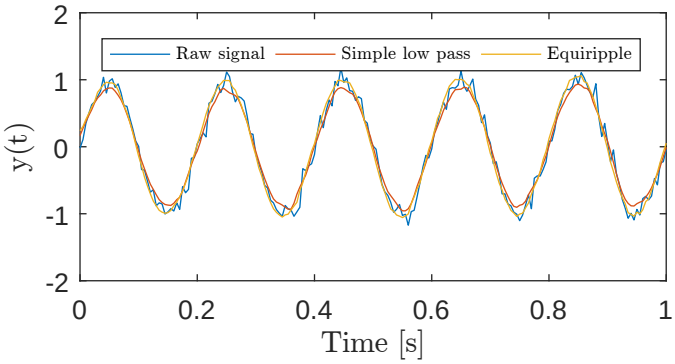

Figure 2.5: Filter performance

2.4.1 Discrete time Kalman Filter

The algorithm here is adapted from Fossen (2011). The discrete time Kalman Filter can be used to filter out measurement and process noise affecting a system, in addition to online estimating the state of a dynamic system. Consider the following discrete time

system:

$$\mathbf{x}(k+1) = \mathbf{\Phi}(k)\mathbf{x}(k) + \mathbf{\Delta}(k)\mathbf{u}(k) + \mathbf{\Gamma}\boldsymbol{w}(k) \tag{2.15a}$$

$$\mathbf{y}(k) = \mathbf{H}(k)\mathbf{x}(k) + \mathbf{v}(k) \tag{2.15b}$$

where process and measurement noise is introduced as $\mathbf{w}(k)$ and $\mathbf{v}(k)$, with the following properties:

$$E[\mathbf{w}(k)\mathbf{w}^T(k)] = \mathbf{Q}(k) = \mathbf{Q}^T(k) > 0 \qquad E[\mathbf{v}(k)\mathbf{v}^T(k)] = \mathbf{R}(k) = \mathbf{R}^T(k) > 0 \tag{2.16}$$

These matrices are known as design matrices, as they can be tuned to improve the performance of the Kalman Filter estimation. The process and measurement noise is assumed to be uncorrelated and Gaussian distributed noise. Assuming the system is observable, we know have that the Kalman Filter is asymptotically stable and the optimal state observer, with minimum variance in the estimate. The Kalman Filter algorithm is summarized in the Table 2.1.

Table 2.1: Discrete time Kalman Filter algorithm

Initial conditions	$\bar{\mathbf{x}}(0) = \mathbf{x}_0$ $\bar{\mathbf{P}}(0) = E\left[(\mathbf{x}(0) - \hat{\mathbf{x}}(0))(\mathbf{x}(0) - \hat{\mathbf{x}}(0))^T\right] = \mathbf{P}_0$
Kalman gain matrix	$\mathbf{K}(k) = \bar{\mathbf{P}}(k)\mathbf{H}^T(k)\left[\mathbf{H}(k)\bar{\mathbf{P}}(k)\mathbf{H}^T(k) + \mathbf{R}(k)\right]^{-1}$
State estimate update	$\hat{\mathbf{x}}(k) = \bar{\mathbf{x}}(k) + \mathbf{K}(k)\left[\mathbf{y}(k) - \mathbf{H}(k)\bar{\mathbf{x}}(k)\right]$
Error covariance update	$\hat{\mathbf{P}}(k) = [\mathbf{I} - \mathbf{K}(k)\mathbf{H}(k)]\,\bar{\mathbf{P}}(k)\,[\mathbf{I} - \mathbf{K}(k)\mathbf{H}(k)]^T + \mathbf{K}(k)\mathbf{R}(k)\mathbf{K}^T(k)$
State estimation propagation	$\bar{\mathbf{x}}(k+1) = \mathbf{\Phi}(k)\hat{\mathbf{x}}(k) + \mathbf{\Delta}(k)\mathbf{u}(k)$
Error covariance propagation	$\bar{\mathbf{P}}(k+1) = \mathbf{\Phi}(k)\hat{\mathbf{P}}(k)\mathbf{\Phi}^T(k) + \mathbf{\Gamma}(k)\mathbf{Q}(k)\mathbf{\Gamma}^T(k)$

2.4.2 Adaptive Fading Kalman Filter

As described in the previous subsection, the Kalman Filter provides an optimal estimation of the state when the measurement relation and the model for the system dynamics are perfect. When this is not the case, the filter may learn the wrong state

and thus diverge. In Janabi-Sharifi et al. (2000) a method to account for the imperfections in the model and measurements is presented, namely the Adaptive Fading Kalman Filter. This method introduces a forgetting factor λ on the error covariance propagation, such that the system has less memory of the previous states. The error covariance equation described in Table 2.1 now becomes

$$\bar{\mathbf{P}}(k+1) = \lambda(k)\mathbf{\Phi}(k)\hat{\mathbf{P}}(k)\mathbf{\Phi}^T(k) + \mathbf{\Gamma}(k)\mathbf{Q}(k)\mathbf{\Gamma}^T(k) \tag{2.17}$$

with $\lambda(k) > 1$. The filter performance will strongly depend on the magnitude of the forgetting factor, and thus an algorithm for calculating the optimal forgetting factor is outlined in the paper. However, for this thesis, the forgetting factor was tuned manually to obtain satisfactory performance of the AKF. Hence, the algorithm is not repeated here, and the reader is referred to the literature for further information.

2.5 Discrete differentiation

There exist numerous methods for differentiating a discrete measured signal, and in this section some relevant methods are presented and their performance are compared. One major difference between the methods are whether they are capable of doing online differentiation, or if the method has a time delay and is thus better suited for posterior processing. As mentioned in Section 2.3.1, using a FIR filter implies a time delay and thus they are better suited for posterior analysis. One major issue with differentiation of a discrete signal with measurement noise is that the noise is severely amplified using a direct method. Given a sampled signal $y(k) = x(k) + e(k)$, where $x(k)$ is the true state and $e(k)$ is the measurement error at sample k. Now, using the finite difference method based on Euler approximation, the derivative is found as

$$v(k) = \frac{\Delta y}{\Delta t} = \frac{x(k) - x(k-1)}{T} + \frac{e(k) - e(k-1)}{T} \tag{2.18}$$

where T is the sampling period. In MATLAB this derivation is done by using the function *diff.m* and divide by the sampling period. The magnitude of the measurement noise does not vary with sampling frequency, and thus it is clear that the impact of the measurement noise increases exponentially as the sampling period is reduced. As a result, one has to take care when differentiating. Low-pass filtering the sampled signal is one method, with the objective of removing the measurement noise and then calculating the derivative as in equation (2.18). In MATLAB it is also possible to design a differentiatior FIR filter, that differentiates the signal as described by Mathworks (2017b). The third method studied here is the possibility of using an AKF to estimate the derivate of the signal, based on a simple system. Compared to the first two methods, this one has the possibility of estimating the derivative of the signal in real-time, and is thus better suited for online calculations. Consider the following discrete time system:

$$\mathbf{x}(k+1) = \mathbf{A}\mathbf{x}(k) \tag{2.19a}$$

$$y(k) = \mathbf{H}\mathbf{x}(k) \tag{2.19b}$$

where $\mathbf{x} = [x\ \dot{x}\ \ddot{x}]^T$ is the state variable. The system matrices are

$$\mathbf{A} = \begin{bmatrix} 1 & \mathrm{T} & \frac{1}{2}T^2 \\ 0 & 1 & \mathrm{T} \\ 0 & 0 & 1 \end{bmatrix} \qquad \mathbf{H} = \begin{bmatrix} 1 & 0 & 0 \end{bmatrix}$$

Using a Kalman Filter to estimate the states, it is possible to model the actual changes in the system as a stationary random process. This is done by adding white noise as a surrogate in the acceleration, such that the equation for changes in acceleration is $\ddot{x}(k+1) = \ddot{x}(k) + w$. Obviously this model does not perfectly represent the motions of a vessel, and thus the forgetting factor in the Kalman Filter is used to eliminate the effect of older data.

2.5.1 Performance of methods

The performance of the different methods are compared using a sampled signal of the yaw angle measured by Qualisys, with a sampling frequency of 100 Hz. The filter parameters were set to:

- **Differentiatior** Filter order = 50, Passband frequency = 2 Hz, Stopband frequency = 5 Hz.
- **Low pass** Passband frequency = 2 Hz, Stopband frequency = 5 Hz, Passband attenuation = 0.5 dB, Stopband attenuation = 100 dB.
- **AKF** Process noise = $10^{-3.5}$, Measurement noise = 0.005, Forgetting factor = 1.2

The sampled signal is presented in Figure 2.6, together with the calculated accelerations using the four methods described above. It should be noted that for illustrative purpose, the time delay has been accounted for in the filtered accelerations. It is clear that direct differentiation of the signal is highly affected by the measurement noise, and is not a feasible method. For the three methods using filters, all of them show similar behavior. The AKF shows some oscillatory effects, and does not estimate the same magnitude of the peaks. It is also seen that the differentiator filter show some tendency of the noise. The low pass filter has the smoothest curve, while it does not have quite the same peaks as the differentiator. As knowledge of the true angular acceleration is not available, the angular rate of each technique is compared to the measured rate by the IMUs onboard. The true angular rate is calculated as the average of the four IMU's, after the signal has been low pass filtered to remove noise. These results are illustrated in Figure 2.7, also here the time delay has been accounted for. It is clear that both the differentiator and low pass filter does a good job in estimating the angular velocity, and it is seen that the measured angular rate has a smooth curve. Hence, for further analysis in this thesis, the low pass differentiation method is used to estimate the derivative of a discrete signal. The AKF method is not satisfactory, but one important aspect is that there has been no correction for time-delay plotting this estimate. For applications where online estimate of the derivative is needed, the AKF might be a

good solution. The performance of the filter might also improve by implementing the optimal forgetting factor, as mentioned in section 2.4.2.

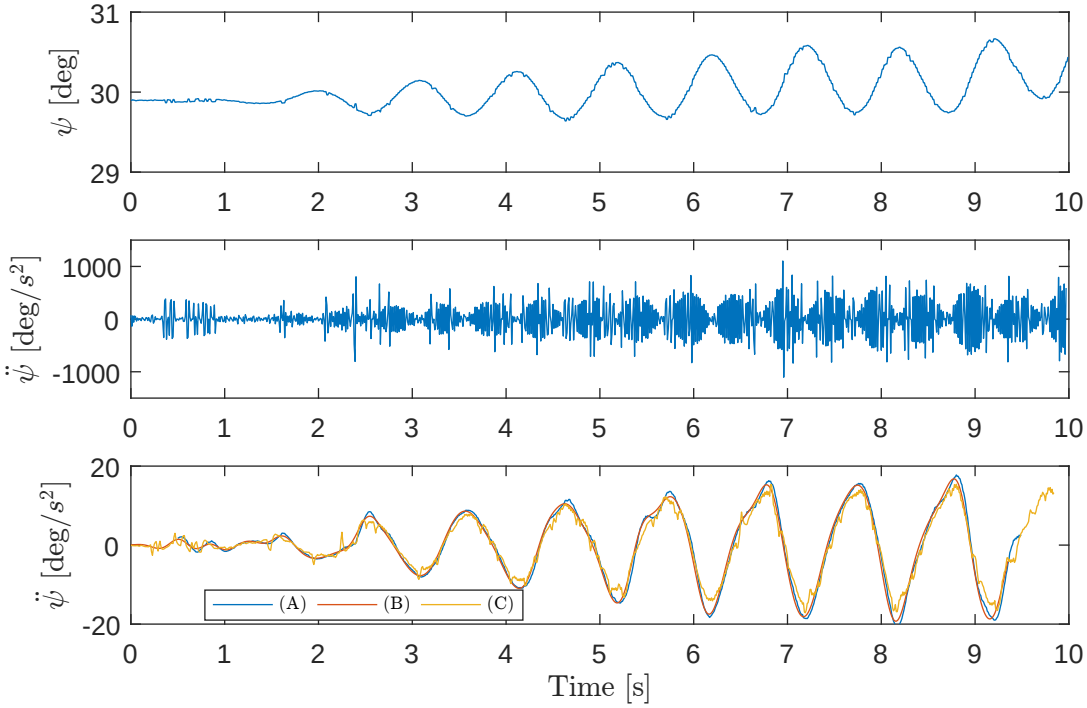

Figure 2.6: Upper figure shows measured yaw angle, and middle figure shows acceleration using *diff.m* without filtering. Lower figure shows estimated acceleration using the different techniques, where (A) is differentiator filter, (B) is low pass filter and (C) is Adaptive fading Kalman Filter

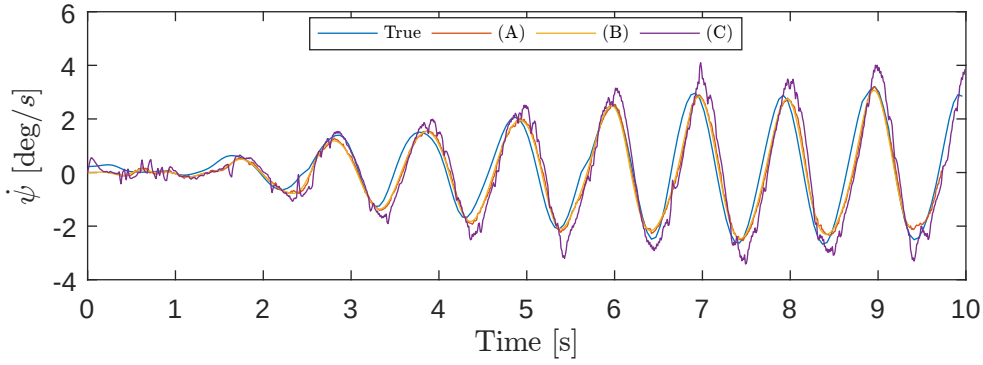

Figure 2.7: Measured angular rate from IMUs and estimated rates

Chapter 3

Motion estimation

3.1 Problem statement

In this chapter two separate problems are solved:

- Estimate linear and rotational accelerations in Center of Origin(CO)
- Estimate linear accelerations in each sensor frame origin(SO)

The kinematic equations of motion for both problems are modeled as an LTV system, given as

$$\dot{\mathbf{x}} = \mathbf{A}(t)\mathbf{x} + \mathbf{B}\mathbf{u} \tag{3.1a}$$

$$\mathbf{y} = \mathbf{H}\mathbf{x} \tag{3.1b}$$

where $\mathbf{A}(t)$ and $\mathbf{B}$ are the system matrices defined for each problem in the next sections, and $\mathbf{H}$ is a selection matrix. Using the notation defined in Section 2.1.2, i.e. subscript *b/f* means o_b with respect to o_f and the superscript denotes which frame it is expressed in, the state variables, inputs and outputs for each problem are:

CO The state vector is $\mathbf{x} := \text{col}(\mathbf{p}^b_{b/f}, \mathbf{v}^b_{b/f}, \mathbf{g}^b, \boldsymbol{\omega}^b_{b/f}) \in \mathbb{R}^{12}$, the input is $\mathbf{u} := \text{col}(\mathbf{a}^1_m, \mathbf{a}^2_m, \mathbf{a}^3_m, \mathbf{a}^4_m) \in \mathbb{R}^{12}$, where $\mathbf{a}^i_m \in \mathbb{R}^3$, $i = 1, ..., 4$, are measured accelerations from the *i*'th IMU. The system outputs are $\mathbf{y} := \mathbf{p}^b_{b/f} \in \mathbb{R}^3$.

SO The state vector is $\mathbf{x}_i := \mathbf{col}(\mathbf{p}^{si}_{si/f}, \mathbf{v}^{si}_{si/f}, \mathbf{g}^{si}) \in \mathbb{R}^9$. The inputs are $\mathbf{u}_i := \mathbf{a}^{si}_m \in \mathbb{R}^3$, and the outputs are $\mathbf{y}_i := \mathbf{p}^{si}_{si/f} \in \mathbb{R}^3$.

The objective for each problem is stated as

- Estimate linear accelerations in CO, $\mathbf{a}_{CO} = \dot{\mathbf{v}}^b_{b/f}$, and rotational accelerations in CO, $\boldsymbol{\alpha}_{CO} = \dot{\boldsymbol{\omega}}^b_{b/f}$.

- Estimate linear accelerations in SO for the i'th IMU, $\mathbf{a}^i_{SO} = \dot{\mathbf{v}}^i_{i/f}$.

3.2 Estimation of linear accelerations in CO

Estimating linear accelerations in CO may be done in several ways, and obviously the easiest would be to simply mount an IMU in CO and directly measure the accelerations. However, this is in many cases not possible due to spacial limitations. One more feasible solution is to mount an IMU at a chosen location, and translate the accelerations to CO. However, this would require knowledge of the angular accelerations, which are not measured with a standard measurement device used in marine application. In this section, a solution for estimating the accelerations in CO is presented, based on the derivations in Kjerstad and Skjetne (2016). In Batista et al. (2011a) the measured accelerations in one IMU is modeled as

$$\mathbf{a}_m = \mathbf{a}_l + \boldsymbol{\omega} \times \mathbf{v} - \mathbf{g} + \mathbf{b} + \mathbf{w} \tag{3.2}$$

where $\mathbf{a}_m \in \mathbb{R}^3$ is the sensor output, $\mathbf{a}_l \in \mathbb{R}^3$ is the linear accelerations in the sensor mounting point, $\mathbf{g} \in \mathbb{R}^3$ is the gravitational vector, $\mathbf{b} \in \mathbb{R}^3$ is the sensor bias and $\mathbf{w} \in \mathbb{R}^3$ is white measurement noise. In an inertial coordinate frame the acceleration of gravity is assumed constant, and thus its time derivative can be modeled as

$$\dot{\mathbf{g}} = -\boldsymbol{\omega} \times \mathbf{g} \tag{3.3}$$

The relation between the measured linear accelerations in the sensor mounting point and the accelerations in CO is given as

$$\mathbf{a}_l = \mathbf{a}_{CO} + \boldsymbol{\alpha} \times \boldsymbol{l} + \boldsymbol{\omega} \times [\boldsymbol{\omega} \times \boldsymbol{l}] \tag{3.4}$$

where $\mathbf{a}_{CO} \in \mathbb{R}^3$ is the linear acceleration in CO, $\boldsymbol{\alpha} \in \mathbb{R}^3$ is the angular acceleration and $\boldsymbol{l} := \text{col}(l_x, l_y, l_z)$ is the lever arm from o_b to o_s expressed in {b}. The linear acceleration in o_s can now be parametrized as one static and one dynamic part:

$$\begin{aligned} \mathbf{a}_l &= \begin{bmatrix} \mathbf{I}_{3\times 3} & \mathbf{S}(\boldsymbol{l})^T & \mathbf{H}(\boldsymbol{l}) \end{bmatrix} \begin{bmatrix} \mathbf{a}_{CO} \\ \boldsymbol{\alpha} \\ \bar{\boldsymbol{\omega}} \end{bmatrix} \\ &= \mathbf{W}(\boldsymbol{l})\mathbf{z} \end{aligned} \tag{3.5}$$

where $\mathbf{I}_{3\times 3} \in \mathbb{R}^{3\times 3}$ is the identity matrix, $\mathbf{S}(\boldsymbol{l})$ is the skew symmetric cross-product matrix from (2.7). $\mathbf{H}(\boldsymbol{l})$ is defined as

$$\mathbf{H}(\boldsymbol{l}) = \begin{bmatrix} 0 & -l_x & -l_x & l_y & l_z & 0 \\ -l_y & 0 & -l_y & l_x & 0 & l_z \\ -l_z & -l_z & 0 & 0 & l_x & l_y \end{bmatrix} \tag{3.6}$$

Finally, the angular rate cross product vector $\bar{\boldsymbol{\omega}}$ is defined as

$$\bar{\boldsymbol{\omega}} = \begin{bmatrix} p^2 & q^2 & r^2 & pq & pr & qr \end{bmatrix}^T \tag{3.7}$$

such that $\mathbf{z} = \text{col}(\mathbf{a}_{CO}, \boldsymbol{\alpha}, \bar{\boldsymbol{\omega}})$. The objective is now to calculate $\mathbf{z}$, however as $\mathbf{W}(\boldsymbol{l}) \in \mathbb{R}^{3\times 12}$ is not invertible, this is solved by augmenting (3.5) to include four IMUs:

$$\begin{aligned} \begin{bmatrix} \mathbf{a}_l^1 \\ \mathbf{a}_l^2 \\ \mathbf{a}_l^3 \\ \mathbf{a}_l^4 \end{bmatrix} &= \begin{bmatrix} \mathbf{W}(\boldsymbol{l}_1) \\ \mathbf{W}(\boldsymbol{l}_2) \\ \mathbf{W}(\boldsymbol{l}_3) \\ \mathbf{W}(\boldsymbol{l}_4) \end{bmatrix} \mathbf{z} \\ \mathbf{a}_{lc} &= \mathbf{G}(\boldsymbol{l}_c)\mathbf{z} \end{aligned} \tag{3.8}$$

where $\mathbf{a}_{lc} \in \mathbb{R}^{12}$ is the combined linear accelerations in each sensor mounting point, $\mathbf{G}(\boldsymbol{l}_c) \in \mathbb{R}^{12\times 12}$ is the static sensor configuration matrix and $\boldsymbol{l}_c := \text{col}(\boldsymbol{l}_1, \boldsymbol{l}_2, \boldsymbol{l}_3, \boldsymbol{l}_4)$ is the lever arm vector for all IMUs. If the sensors are mounted such that at least one of them are outside the plane of the others, i.e. non-coplanar positioning, the system configuration matrix is nonsingular and invertible, as described by Zappa et al. (2001). By augmenting (3.2) to include all four sensors, and inserting (3.8) gives

$$\mathbf{G}(\boldsymbol{l}_c)^{-1}\mathbf{a}_{mc} = \mathbf{z} + \mathbf{G}(\boldsymbol{l}_c)^{-1}\begin{bmatrix} \boldsymbol{\omega}^b_{b/f} \times \mathbf{v}^b_{b/f} - \mathbf{g}^b + \mathbf{b}_{s1} + \mathbf{w}_{s1} \\ \boldsymbol{\omega}^b_{b/f} \times \mathbf{v}^b_{b/f} - \mathbf{g}^b + \mathbf{b}_{s2} + \mathbf{w}_{s2} \\ \boldsymbol{\omega}^b_{b/f} \times \mathbf{v}^b_{b/f} - \mathbf{g}^b + \mathbf{b}_{s3} + \mathbf{w}_{s3} \\ \boldsymbol{\omega}^b_{b/f} \times \mathbf{v}^b_{b/f} - \mathbf{g}^b + \mathbf{b}_{s4} + \mathbf{w}_{s4} \end{bmatrix} \tag{3.9}$$

where $\mathbf{a}_{mc} := \text{col}(\mathbf{a}^1_m, \mathbf{a}^2_m, \mathbf{a}^3_m, \mathbf{a}^4_m)$. By considering this as a deterministic input to the state-space model in (3.1), we may design an observer to estimate the accelerations in CO. Using the kinematic model from (2.6), the model for this problem becomes

$$\dot{\mathbf{p}}^b_{b/f} = -\mathbf{S}(\boldsymbol{\omega}^b_{b/f})\mathbf{p}^b_{b/f} - \mathbf{v}^b_{b/f} \tag{3.10a}$$

$$\dot{\mathbf{v}}^b_{b/f} = -\mathbf{S}(\boldsymbol{\omega}^b_{b/f})\mathbf{v}^b_{b/f} - \mathbf{g}^b - \mathbf{b}_l + \mathbf{B}_1\mathbf{G}(\boldsymbol{l}_c)^{-1}\mathbf{a}_{mc} \tag{3.10b}$$

$$\dot{\mathbf{g}}^b = -\mathbf{S}(\boldsymbol{\omega}^b_{b/f})\mathbf{g}^b \tag{3.10c}$$

$$\dot{\mathbf{b}}_l = \mathbf{0} \tag{3.10d}$$

$$\dot{\boldsymbol{\omega}}^b_{b/f} = \mathbf{b}_\omega + \mathbf{B}_2\mathbf{G}(\boldsymbol{l}_c)^{-1}\mathbf{a}_{mc} \tag{3.10e}$$

$$\dot{\mathbf{b}}_\omega = \mathbf{0} \tag{3.10f}$$

where $\mathbf{B}_1, \mathbf{B}_2 \in \mathbb{R}^{3\times 12}$ are selection matrices for $\mathbf{a}_{CO}$ and $\boldsymbol{\alpha}$ in (3.5), respectively. In (3.10) two bias terms are included. The linear bias term, $\mathbf{b}_l \in \mathbb{R}^3$, is added to account for bias in the measured acceleration from the sensors. For the angular acceleration, the objective of the $\boldsymbol{\omega}$ state is to remove bias from the measurements, and thus $\mathbf{b}_\omega \in \mathbb{R}^3$ is added. It is noteworthy that the last term of (3.9) is only corrected for in the linear acceleration estimate. For the angular estimation, it is found that the contribution of the last term is negligible because $\mathbf{B}_2\mathbf{G}(\boldsymbol{l}_c)^{-1}$ multiplied with a repetitive vector such

as $col(\mathbf{g}^b, \mathbf{g}^b, \mathbf{g}^b, \mathbf{g}^b)$ is zero. Hence, it is only the bias and measurement noise that influence the input to the system. The system in (3.10) may now be modeled as an LTV system as given in (3.1), which is solved using the discrete time Kalman Filter described in Section 2.4.1.

3.3 Estimation of linear accelerations in SO

The second problem is to determine local accelerations in the hull, i.e. the accelerations in the origin of each sensor coordinate system. In Batista et al. (2011b) a model for this is outlined. It is similar to the previous method described in Section 3.2, with the measured accelerations working as input to the kinematic model. By subtracting the parts due to gravity and bias one can estimate the local linear accelerations. For sensor *i*, a kinematic model is designed as follows:

$$\dot{\mathbf{p}}^{si}_{si/f} = -\boldsymbol{\omega}^{si}_{si/f} \times \mathbf{p}^{si}_{si/f} - \mathbf{v}^{si}_{si/f} \tag{3.11a}$$

$$\dot{\mathbf{v}}^{si}_{si/f} = -\boldsymbol{\omega}^{si}_{si/f} \times \mathbf{v}^{si}_{si/f} - \mathbf{g}^{si} - \mathbf{b}_{si} + \mathbf{a}^{si}_{m} \tag{3.11b}$$

$$\dot{\mathbf{g}}^{si} = -\boldsymbol{\omega}^{si}_{si/f} \times \mathbf{g}^{si} \tag{3.11c}$$

$$\dot{\mathbf{b}}_{si} = \mathbf{0} \tag{3.11d}$$

where $\mathbf{p}^{si}_{si/f} = \mathbf{R}^b_f(\boldsymbol{\Theta}_{fb})\mathbf{p}^b_{b/f} - \boldsymbol{l}_i$ is the position of o_{si} with respect to o_f expressed in {si}, $\mathbf{v}^{si}_{si/f}$ is the velocity of the sensor. Gravity and bias are as in the previous method. The measured acceleration $\mathbf{a}^i_m$ is given in (3.2). This is now modeled as an LTV system, and solved using the discrete time Kalman Filter.

3.4 Method of validation

The estimated accelerations in Section 3.2 should be validated in some way, to make sure the method has satisfactory performance. From Qualisys, the position and orientation of the vessel is given with high precision. By differentiating these values twice using the method of Section 2.5, one obtain an estimate of the translational and rota-

tional acceleration in CO. The method may be summarized as follows:

$$\mathbf{v}^b_{b/f}(k) = \mathbf{R}^b_f(\boldsymbol{\Theta}_{fb})\left(\mathbf{p}^f_{b/f}(k) - \mathbf{p}^f_{b/f}(k-1)\right)/T \tag{3.12a}$$

$$\mathbf{a}^b_{b/f}(k) = \left(\mathbf{v}^b_{b/f}(k) - \mathbf{v}^b_{b/f}(k-1)\right)/T \tag{3.12b}$$

$$\boldsymbol{\omega}^b_{b/f}(k) = \mathbf{T}^{-1}_{\Theta}(\boldsymbol{\Theta}_{fb})\left(\boldsymbol{\Theta}_{fb}(k) - \boldsymbol{\Theta}_{fb}(k-1)\right)/T \tag{3.12c}$$

$$\boldsymbol{\alpha}^b_{b/f}(k) = \left(\boldsymbol{\omega}^b_{b/f}(k) - \boldsymbol{\omega}^b_{b/f}(k-1)\right)/T \tag{3.12d}$$

These calculated accelerations are used to evaluate the estimates of the acceleration in CO. (3.4) is used by to calculate the linear accelerations in SO as both rotational rate and acceleration are assumed known from (3.12). Thus, the linear accelerations in SO for IMU i is calculated as

$$\mathbf{a}^i_l(k) = \mathbf{a}^b_{b/f}(k) + \boldsymbol{\alpha}^b_{b/f}(k) \times \boldsymbol{l}_i + \boldsymbol{\omega}^b_{b/f}(k) \times \left[\boldsymbol{\omega}^b_{b/f}(k) \times \boldsymbol{l}_i\right] \tag{3.13}$$

3.5 Estimation of direction of incoming waves

Three methods for estimating the direction of incoming waves are proposed in this thesis:

1. Analyze correlation between motion in roll, pitch and yaw for different direction of incoming waves

2. Analyze spatially distributed accelerations in surge and sway to determine where the waves hit the vessel

3. Analyze spatially distributed accelerations in heave over time as waves travel through the vessel

The first two methods are generally based on analysis of the experimental results, while the third is an analytical approach based on the properties of waves. In the latter, a brief description of each method is given.

3.5.1 Motion in roll, pitch and yaw

This method is inspired from the approach of Tannuri et al. (2003), where comparison between vessel response with its pre-calculated RAO for different headings is used to estimate the direction of incoming waves. It is well known that a vessel have different behavior depending on the direction of incoming waves, due to the non-symmetric hull shape in the y-z plane. Hence, by investigating the phase difference between motion in roll, pitch and yaw, one might find some correlation between the hull motion and the direction of incoming waves.

3.5.2 Accelerations in surge and sway

Full scale ships are in general built of steel, and they are flexible structures. Phenomenas like sagging and hogging are examples of hull flexibility as a result of the design. With this in mind, it is proposed to investigate spatially distributed accelerations in surge and sway to determine if the hull absorb some of the wave energy. This method relates to the lateral-line sensing problem, which is based on pressure difference between port and starboard. Potentially, if such decay in energy is found, one can obtain knowledge of the surrounding force field and direction of incoming waves.

3.5.3 Accelerations in heave

The final method proposed is based on the force distribution in the hull as waves travel through it. As described in Section 4, the experiments carried out in this thesis are done with Stoke's 1st order regular waves. With the assumptions described in Section 1.3, i.e. deep water, according to Faltinsen (1993) the dispersion relation is given as

$$\frac{\omega^2}{g} = k \tag{3.14}$$

where $\omega = 2\pi/T$ is the circular wave frequency, g is the acceleration of gravity, $k = 2\pi/\lambda$ is the wave number and λ is the wave length. Further, the phase velocity of the

wave is

$$c = \frac{\omega}{k} \tag{3.15}$$

Substituting for the wave number, the velocity can be described in terms of the period

$$c = \frac{g}{\omega} = \frac{gT}{2\pi} \tag{3.16}$$

Thus, with knowledge of the wave period it is possible to calculate the velocity of the wave through the hull. The position of each sensor is given in Chapter 4, and here a method for estimating the direction of incoming waves is proposed based on the spatial position of each sensor. Let IMU #1 be the reference sensor, such that all other IMU data are relative to this sensor. As an example, consider the pair consisting of IMU #1 and #3. The distance between them in the horizontal plane is given by the vector $\mathbf{p}^{s1}_{s3/s1}$, and thus the time it takes for one wave to travel from one IMU to the other is given as a function of the direction of incoming wave relative to their orientation. The estimated time difference is calculated as

$$t_e(\beta) = \frac{distance}{velocity} = \frac{\left\|\mathbf{p}^{s1}_{s3/s1}\right\| \cos\left(\psi_{s3/s1} - \beta\right)}{c} \tag{3.17}$$

where $\psi_{s3/s1}$ is the angle to {s3} expressed in {s1} and β is the direction of the incoming waves expressed in {s1}. See Figure 3.1 for an illustration. Note that β is defined as the direction of the incoming waves, thus a positive heading of the vessel in the basin, e.g. $\psi = 10^o$, correspond to a negative direction of incoming waves, i.e. $\beta = -10^o$. Further, by measuring the point in time of the extrema in heave acceleration for both sensors, one obtain a measurement of the time t_m the wave traveled between the two sensors. The direction of incoming waves may now be estimated by optimizing the angle β to get the best correspondence with measured value. Expressed mathematically, the objective is to minimize the difference in time:

$$\underset{\beta \in (-180^o, 180^o]}{\text{minimize}} \qquad t_e(\beta) - t_m \tag{3.18}$$

By augmenting this method to include all four sensors, it is possible to get a unique combination for each direction of incoming waves. In Figure 3.2 the estimated time difference between IMU#1 and the other IMUs for different direction of incoming waves is shown. The objective of minimizing the time difference then becomes an optimization problem in the least squares sense.

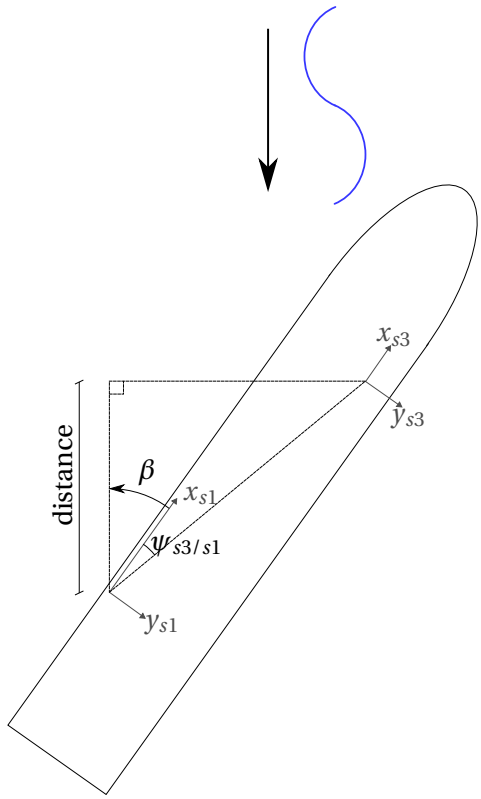

Figure 3.1: Estimating direction of incoming waves

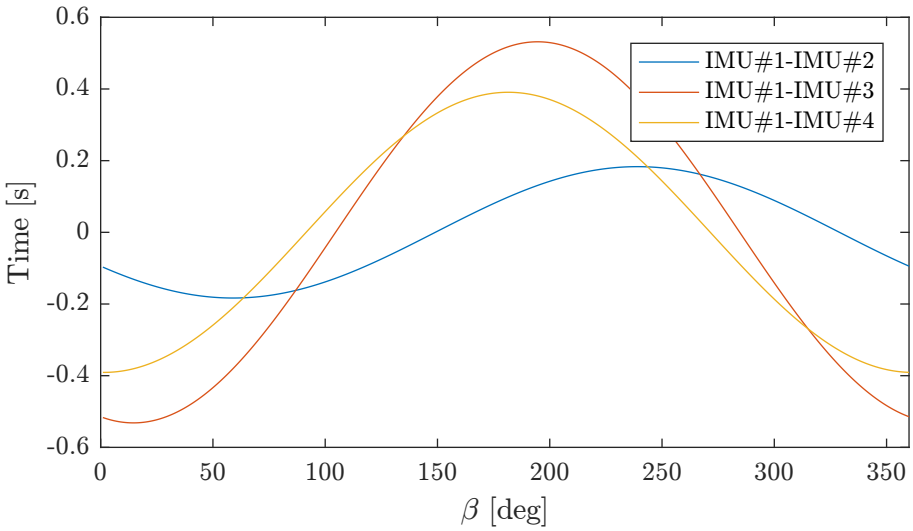

Figure 3.2: Modeled time difference in heave acceleration extrema between sensors

Chapter 4

Instrumentation and experimental setup

4.1 Marine Cybernetics Laboratory

All experiments were carried out in the Marine Cybernetics Laboratory (MCLab), located at the Institute of Marine Technology in Trondheim, Norway. The laboratory facilitates several experimental setups, for both navigation on and under the water surface. In Handbook (2016) a detailed description on the laboratory is given, and the relevant information is presented here. The lab has one basin with length 40 meters, breadth 6.45 meters and depth 1.5 meters. At one of the ends there is a beach, while at the other there is a single paddle wave generator. The lab also has a towing carriage with a system for motion tracking on the surface, namely Qualisys Motion Tracker. The basin is illustrated in Figure 4.1, with positive directions of the basin frame set up by Qualisys.

Wave generator

The wave generator can produce several wave spectra, including Stoke's 1st order regular waves. The basin can create regular waves with significant wave height up to $0.25[m]$, and period T from $0.3-3.0[s]$. The objective of the beach at the opposite end

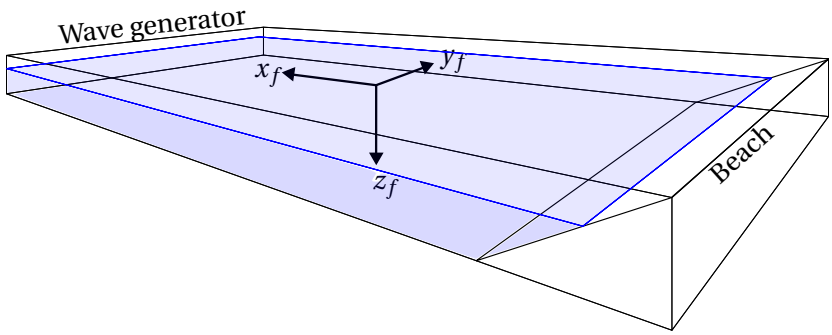

Figure 4.1: Basin illustration, with definition of {f}

from the wave generator is to remove the wave energy such that the waves are not reflected back. However, due to some temporary modifications in the basin, the beach was not properly working during the experiment and thus the waves were partly reflected. This restricted how long the experiments were run, as it was desirable to only analyze regular waves.

Qualisys Motion Tracker

The Qualisys Motion Capture System used in the lab is a setup of three Oqus high speed infrared cameras, such that the system is capable of tracking motion in 6 DOFs. The cameras register the position of the infrared reflectors mounted on top of the model, and translate them to one point defined by the user, called CO in this thesis. The point is defined by a vector relative the highest reflector r, $\mathbf{p}^f_{b/r} = [960, -190, -575]$ $[mm]$. The system has millimeter precision, and the sampling rate is set to 50 Hz. The position and orientation of the vessel, $\mathbf{p}^f_{b/f}$ and $\mathbf{\Theta}_{fb}$, are broadcasted over WiFi for processing onboard. It should be noted that the standard convention for rotations in Qualisys is *xyz*, as described in Qualisys (2011). Hence, some corrections are necessary to obtain the Euler angles according to the *zyx*-convention. Given the Euler angles

from Qualisys using *xyz*, $\mathbf{\Theta}'_{fb} = [\phi', \theta', \psi']$, the rotation matrix can be calculated as:

$$\mathbf{R}^{f}_{b,xyz}(\mathbf{\Theta}'_{fb}) = \begin{bmatrix} c\theta' c\psi' & -c\theta' s\psi' & s\theta' \\ c\phi' s\psi' + c\psi' s\phi' s\theta' & c\phi' c\psi' - s\phi' s\theta' s\psi' & -c\theta' s\phi' \\ s\phi' s\phi' - c\phi' c\psi' s\theta' & c\psi' s\phi' + c\phi' s\theta' s\psi' & c\phi' c\theta' \end{bmatrix} \tag{4.1}$$

By utilizing the fact that the rotation matrices from both the *xyz*- and *zyx*-convention are equal, $\mathbf{R}^{f}_{b,zyx}(\mathbf{\Theta}_{fb}) = \mathbf{R}^{f}_{b,xyz}(\mathbf{\Theta}'_{fb})$, it is possible to calculate the Euler angles according to the *zyx*-convention. In the free MATLAB toolbox of Fossen and Perez (2004), the function *R2euler.m* computes the Euler angles in *zyx*-convention from the rotation matrix.

4.2 C/S Inocean Cat I Drillship

The model used in these experiments is the C/S Inocean Cat I Drillship (CSAD), which is the newest contribution to the Cybership fleet in the MCLab. The model was built and instrumented in 2016 as described in Bjørnø (2016), and the objective of the new model was to arrange for more research on TAPM. The ship model is based on Statoil's Cat I Arctic Drillship, and is a 1:90 scaled version. It is equipped with six azimuth thrusters, three fore and three aft. The hull is also enabled for use of a freely rotating turret for positioning with mooring lines. The main dimensions of the scaled model are presented in Table 4.1. CSAD is the largest boat in the Cybership fleet, and offers more flexibility for sensor placement inside the hull, which is desirable for the experiments carried out in this thesis. Figure 4.2 shows the model boat in the basin during one experiment, with heading equal 150^o.

Table 4.1: Main dimensions of CSAD

Parameter	**Value**[m]
Length over all	2.578
Breadth	0.440
Depth moulded	0.211
Design draught	0.133

Figure 4.2: Photo of CSAD with $\psi = 150^o$

4.3 Hardware

4.3.1 Inertial Measurement Units

There are a variety of instruments for measuring inertial forces available on the market, from low-cost units such as the ones installed in smartphones to high-end units intended for professional use. The sensors used in this thesis are the *ADIS16364*, manufactured by Analog Devices, and includes a triaxis gyroscope and triaxis accelerometer. Each sensor has built-in compensation for bias, alignment and sensitivity, and thus provides accurate measurements over a temperature range of -10^oC to $+70^oC$. The main data relevant for this thesis is presented in Table 4.2, and for supplementary information the reader is referred to the data sheet Analog Devices (2017). The sensor is mounted on a breakout board, as shown in Figure 4.3b, for communication with the microprocessor described in the next Section. The sensors also have built-in bias calibration.

4.3.2 Arduino Leonardo ETH

Each IMU were connected to a microprocessor for sampling of the sensor data. The Arduino Leonardo ETH microprocessor was chosen, as this has SPI-interface for connecting to the IMU and a built-in Ethernet module for network communication. Figure 4.3a shows a photo of the microprocessor. The Arduino Leonardo ETH enables higher spatial freedom for installation of the sensors, as they can communicate over

Table 4.2: IMU specifications

	Parameter	Typical value	Unit
Gyroscopes	Dynamic range	±350	^{o}/sec
	Sensitivity	0.0125	^{o}/sec/LSB
	Bias stability, σ	0.007	^{o}/sec
	Angular random walk	2.0	$^o/\sqrt{hr}$
	Output noise	0.8	^{o}/sec rms
Accelerometers	Dynamic range	±5.25	g
	Sensitivity	1.00	mg/LSB
	Bias stability, σ	0.1	mg
	Velocity random walk	0.12	m/sec/$\sqrt{hr}$
	Output noise	5	mg rms
Power supply	Operating voltage	5.0 ± 0.25	V

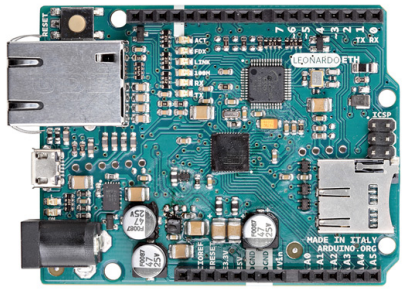

(a) Image of Arduino Leonardo ETH. Courtesy of Arduino (2017)

(b) ADIS16364 mounted on breakout board

Figure 4.3: Images of hardware components

Ethernet with minimum time delay. The Arduino board can operate on input voltage of 6 to 20 volts, with recommended region between 7-12 volts. The vessel is powered on six 12V batteries, and thus the Arduinos can be connected directly to the power grid. The board has 5V output, which is used for powering the IMU. For more technical specifications on the board, the reader is referred to Arduino (2017). In Appendix A.2 the wiring diagram for the microprocessor and breakout board is given. The Arduino and IMU were mounted on a custom made metal sheet designed to fit within small watertight boxes. Figure 4.4 shows a photo of the final setup, without the box lid.

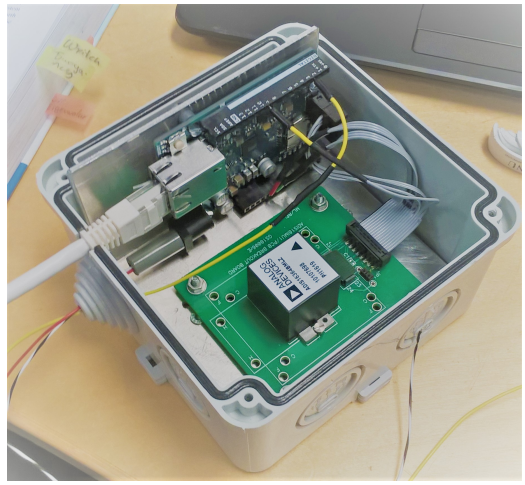

Figure 4.4: Arduino and IMU mounted inside box

4.3.3 CompactRIO

The C/S Inocean Cat I DrillShip model is equipped with a National Instruments CompactRIO-9024, which is an embedded real-time controller. It has several ports for communication, including two Ethernet ports. It is also connected to several modules for control purposes, as described in Bjørnø (2016). There is one WiFi-bridge mounted onboard enabling wireless connection to the cRIO, such that the cRIO can receive broadcasted motion data from Qualisys. Depending on the application, programming the controller can be done using LabVIEW or Simulink code exported to C-language with National Instruments plug-in.

4.4 Software

In order to sample the IMU data and process it on the cRIO, different software was designed. In this section a short description of the software for communication between the different hardware parts is given. Figure 4.5 illustrates the system configuration between the different parts.

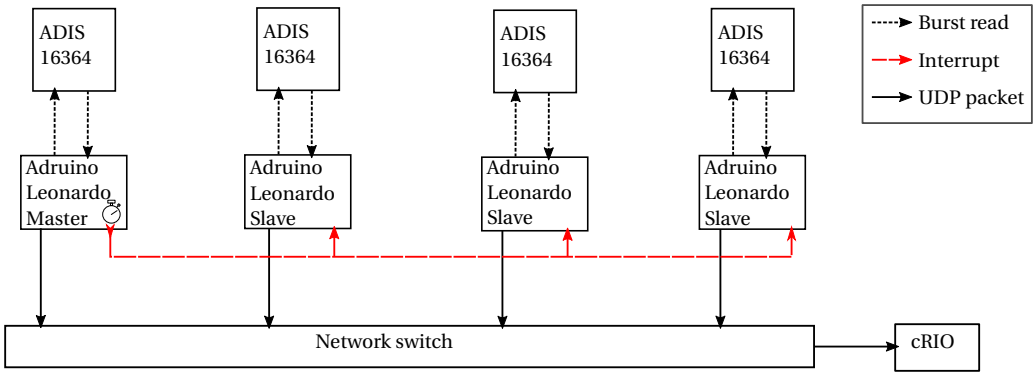

Figure 4.5: System schematic of hardware communication

4.4.1 Reading data from IMU

The IMU produces inertial measurements data at a sampling rate of 819.2 SPS , and load it to an output register. In operation, the IMU operates as a slave, and the Arduino operates as the master. Communication with the IMU is done through 16-bit segments, and thus the Arduino must send 16-bit messages to request data to read. The Arduino is well suited for this purpose, as it is easily configurable to send desired messages through the SPI bus. There are several ways of requesting measurements from the IMU, e.g. it is possible to request a specific measurement or do a burst read of all measurements. In Gleason (2013) an example code for interfacing Arduino with an ADIS16364 is given, with necessary libraries. Some minor adjustments had to be made, due to some distinction between the different Arduino models. The libraries include code for performing a burst read of the sensor data, which was chosen for this purpose. After sending a burst read message to the IMU, the Arduino reads the instant sensor data: three-axial accelerations, rotations and temperatures in addition to sensor voltage as binary message. The code provides necessary scaling of the data to float numbers. The Arduino is now ready to send the data to a recipient, namely the cRIO.

4.4.2 Sending data from Arduino to cRIO

Transmitting data from the Arduino to the cRIO is done using Ethernet communication. A variety of protocols for network communication exists, and the two most com-

mon ones are TCP and UDP , as given in Fall and Stevens (2011). The main difference between them is that the TCP is based on a two-way communication between the sender and recipient, while the UDP is a one-way system. This means that there is no verification on whether the UDP packet has been received, thus there may be loss of data. For this application, UDP is the preferred one as the objective is to send packets from the Arduino to the cRIO without any need of sending data back. For transmitting data over Ethernet, the Arduino library provides the necessary code. The Arduino is programmed to send the IMU data to a specified IP-address and port number on the network. The cRIO is configured to continuously listen to this specified port, and read the data when a new packet is received. This configuration was done by creating a custom device module in LabVIEW for the cRIO, see Appendix for further information. The IMU data can now be accessed with Simulink code.

4.5 Time synchronization of sensors

It is of crucial importance that the sampling from the different IMUs are done in the same instance, without any time delay. Several methods for time synchronization exists, e.g. the much used PPS method. As the Arduino has several available digital I/O ports, sending an interrupt signal was chosen for time synchronization between the Arduinos. This was accomplished by programming one Arduino to operate as the master, which sends an interrupt signal to the other Arduinos with a desired frequency. Once the slave receives the interrupt signal, it reads the IMU data and sends it to the cRIO. A simple experiment was set up to verify the quality of the interrupt signal as time synchronization method. The setup is illustrated in Figure 4.6, and a force was applied on the end of the plate such that the plate starts to oscillate. The IMU data was logged on the cRIO, and are presented in Figure 4.7. The presented data are not filtered, and thus are affected by measurement noise which makes it a bit harder to validate the results. As a second method, the raw data were fitted to a curve using a nonlinear least-squares curve fitting tool in MATLAB(*lsqcurvefit.m*). The motion of the sensors is assumed to be a decaying sinusoidal motion with some offset, and the

acceleration in z-direction is modeled as:

$$a_z(t) = ae^{bt}\sin(ct+d)+e \tag{4.2}$$

where a, b, c, d and e are constants that the least-squares function optimize to find the best curve fit. From the results it is clear that the raw data from the IMUs show strong similarities, and the motion is highly synchronized. This is especially clear in the curve fitted results, as the peaks are at the same instant. Thus, it is concluded that the interrupt signal provides good time synchronization between the IMUs.

Figure 4.6: Image of time synchronization experiment setup

4.6 Experimental setup

In this section the experimental setup is described, including setup in the basin and sensor configuration in the hull.

4.6.1 Fixation of model

The experimental setup of the ship model in the basin can be divided into two groups:

- Fixed position and heading
- No fixation

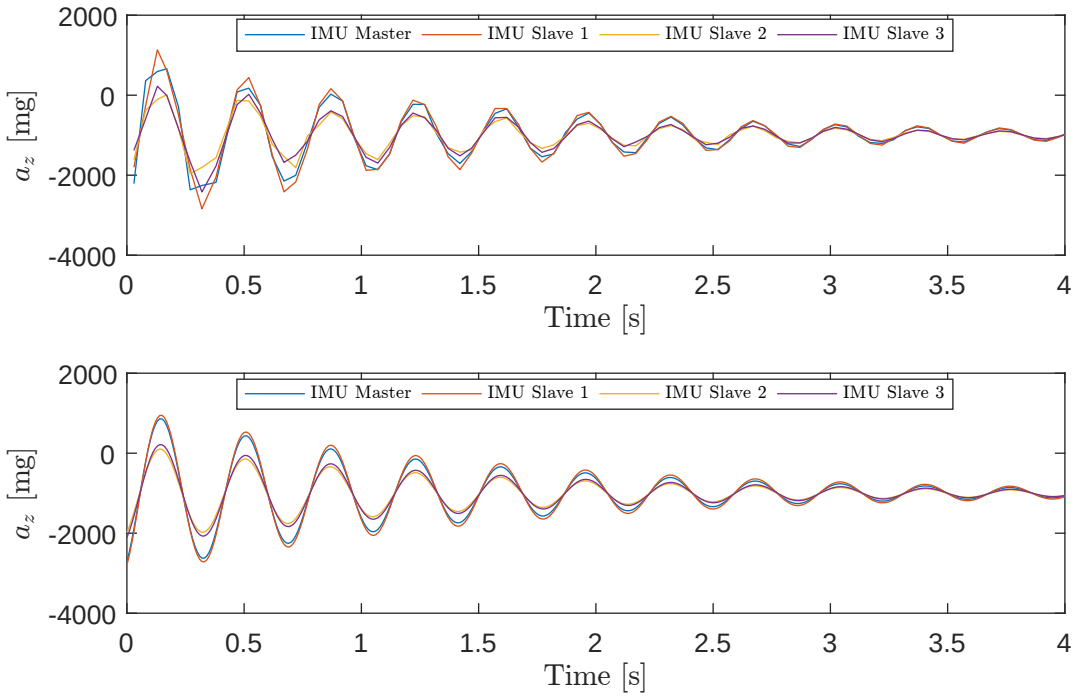

Figure 4.7: Results from time synchronization experiment. Upper figure show raw data from all 4 IMUs, and buttom figure shows results after nonlinear curve fitting.

The setup with position and heading constrained is illustrated in Figure 4.8. The objective of this setup is to make sure that the heading of the vessel does not change, such that it is possible to do analysis of the vessel motion given a specific direction of incoming waves. It should be noted that in this setup, motion in the horizontal plane is strongly limited, and thus the measured accelerations in surge, sway and yaw will be highly influenced by the forces in the straps. However, as these forces are only horizontal, the influence on the motion in heave and pitch will be minimal. The roll motion will to some extent be affected by the constraints, but this is assumed negligible. As seen in Figure 4.8b, at the end of each strap a weight of $1kg$ is attached, which provides the spring effect illustrated in Figure 4.8a.

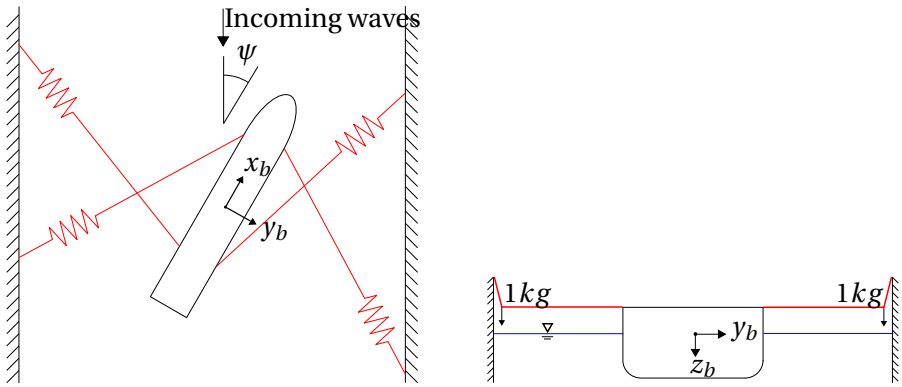

(a) From bird perspective

(b) From fish perspective

Figure 4.8: Illustration of fixation in experiments

4.6.2 Sensor mounting

Two types of sensor configurations were used in the experiments. The different setups are illustrated in Figure 4.9 and 4.10, and their position in the body-frame are presented in Table 4.3 and 4.4. The position was determined by measuring the location from each SO to CO using a folding rule, and thus introduce some measurement errors.

Sensor positions in body-frame

Table 4.3: Sensor configuration 1

IMU #	x[mm]	y[mm]	z[mm]
1	-465	-184	-73
2	-244	184	-13
3	740	130	82
4	450	-160	82

Table 4.4: Sensor configuration 2

IMU #	x[mm]	y[mm]	z[mm]
1	-5	0	-173
2	-1115	0	-173
3	760	0	-173
4	1185	0	-173

In order to translate all forces to CO, the coordinate frames of each sensor must be aligned and parallel with the body frame as described in Kjerstad and Skjetne (2016). However, due to spatial limitations, the sensors had to be mounted with different orientations. Using the *zyx*-convention for rotations, each sensor has an offset from body-frame as given in Table 4.5 and 4.6. These orientations are the optimal ones, i.e. if the sensor frame is parallel to the body frame. The hull has some inclination,

especially the walls which IMU #1 and #2 are mounted on. These inclinations will give some additional contributions to the orientation of the sensor frame relative the body frame. In Won et al. (2010) the initial roll and pitch angle is estimated by comparing the average acceleration measurements relative the gravitational vector when the vessel is not exposed to any forces. Roll and pitch angle offset from the gravitational vector for one sensor is found by:

$$\phi = arctan\left(\frac{Avg_y}{Avg_z}\right) \tag{4.3}$$

$$\theta = arcsin\left(\frac{Avg_x}{\sqrt{Avg_x^2 + Avg_y^2 + Avg_z^2}}\right) \tag{4.4}$$

where Avg_{axis} is the average acceleration of each axis measured by the IMU when the vessel is kept still and horizontal. Obtaining the offset in yaw is a more complex task, and in this thesis it is assumed that the offset is negligible. The rotation matrix in (2.2) can now be used to rotate all sensor frames to be aligned and parallel with the body frame:

$$\mathbf{a}^s_{s/f} = \mathbf{R}^b_{s'}(\boldsymbol{\Theta}_{s'})\mathbf{R}^{s'}_{s''}(\boldsymbol{\Theta}_{s''})\mathbf{a}_m \tag{4.5a}$$

$$\boldsymbol{\omega}^s_{s/f} = \mathbf{R}^b_{s'}(\boldsymbol{\Theta}_{s'})\mathbf{R}^{s'}_{s''}(\boldsymbol{\Theta}_{s''})\boldsymbol{\omega}_m \tag{4.5b}$$

where $\{s\}$ is the body-parallel sensor frame, $\{s'\}$ is frame of initial mounting offset and s'' is the frame of measured roll and pitch offset. $\mathbf{a}_m$ and $\boldsymbol{\omega}_m$ are the raw data from the sensors.

Sensor orientations relative body-frame

Table 4.5: Sensor configuration 1

IMU #	ϕ[deg]	θ[deg]	ψ[deg]
1	-90	0	0
2	-90	0	180
3	180	0	180
4	180	0	0

Table 4.6: Sensor configuration 2

IMU #	ϕ[deg]	θ[deg]	ψ[deg]
1	180	0	180
2	180	0	0
3	180	0	180
4	180	0	180

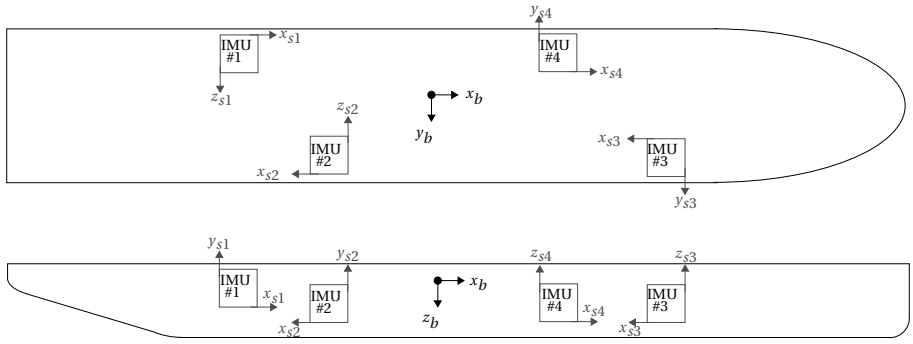

Figure 4.9: Sensor configuration 1

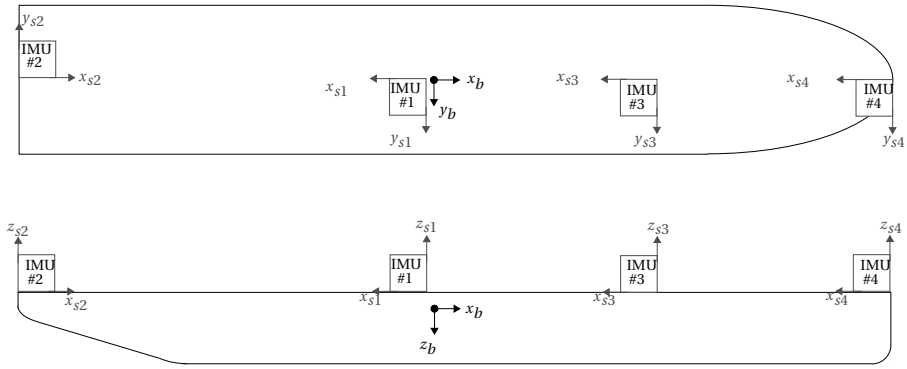

Figure 4.10: Sensor configuration 2

Chapter 5

Experimental data and analysis

5.1 Experiments

Several experiments were carried out, for both sensor configurations described previously. For all experiments, the wave height was set to $H = 0.05[m]$. Table 5.1 gives an overview of which experiments were performed for each sensor configuration, where the numbers 1 and 2 in the cells indicate if the respective sensor configuration was tested for that wave period and fixed heading. The last column, "Free", represent experiments without straps attached such that the vessel was free to drift. The initial heading of the vessel was set to zero degrees for these experiments.

Table 5.1: Overview of experiments carried out

$T[s]$ \ $\psi[deg]$	0	30	60	90	120	150	180	Free
1	1,2	1,2	1	1	1	1,2	1,2	1,2
1.5	1,2	1,2	1	1	1	1,2	1,2	1,2
2	1,2	1,2	1	1	1	1,2	1,2	1,2
2.5	1,2	1,2	1	1	1	1,2	1,2	1,2

Hence, data was sampled from a total number of 52 experiments, and all collected data is provided in the electronic attachment to this thesis. In this chapter, some selected experiments are presented with the objective of evaluating the performance of the two methods of motion estimation presented in Chapter 3. To evaluate the ac-

celeration estimates in CO and SO, sensor configuration 1 with heading fixed to 30 degrees and wave period of 1.5 seconds is chosen. The method of evaluating direction of incoming waves based on phase difference in roll, pitch and yaw is presented for sensor configuration 1, for all wave periods and heading equal 30, 60, 120 and 150 degrees. Estimating the direction of incoming waves based on accelerations in surge and sway is presented for sensor configuration 1, freely floating and wave period of 1 second. Unfortunately the data sampling was stopped once the vessel started to change heading for the free floating experiments, and thus the one that drifts longest is chosen. Further, the proposed method for estimating the direction of incoming waves based on time difference in acceleration peaks is presented with sensor configuration 1, all headings and wave period of 1.5 and 2 seconds. Finally, evaluation of the spatial variability of accelerations in the hull is presented for sensor configuration 2, heading equal 0 and 180 degrees and wave period of 2 seconds.

5.2 Accelerations in CO

Using the method presented in Section 3.2, the accelerations estimated in CO from IMU measurements for a selected heading and wave period is presented here. The process and measurement noise covariance matrices from (2.16) were set based on the actual covariance of the signal with some manual adjustments to improve the filter performance. The true acceleration presented is based on the measurements from Qualisys, as described in Section 3.4. In Figure 5.1 the linear accelerations in surge, sway and heave are presented. The wave train hits the vessel after approximately 15 seconds. Accelerations in surge and sway show some slowly oscillating effects in the estimated accelerations, typically with a period of 20 seconds. This effect is especially clear in sway, as the estimate is a bit lower around 20-25 seconds, a bit higher around 30-35 seconds and then lower again around 40-45 seconds. The estimated heave acceleration are the best, without much deviation from the true value.

In Figure 5.2 the rotational accelerations in roll, pitch and yaw are presented for the same experiment. For roll and pitch the estimated value has a relatively high discrep-

ancy compared to the true acceleration, but is not that prevailing in yaw. The variance of the acceleration in yaw is also much lower than in roll and pitch. By investigating the true acceleration in roll, one can see some strange behavior at the lower values, which is probably caused by the straps constraining the vessel from rolling harmonically with the waves.

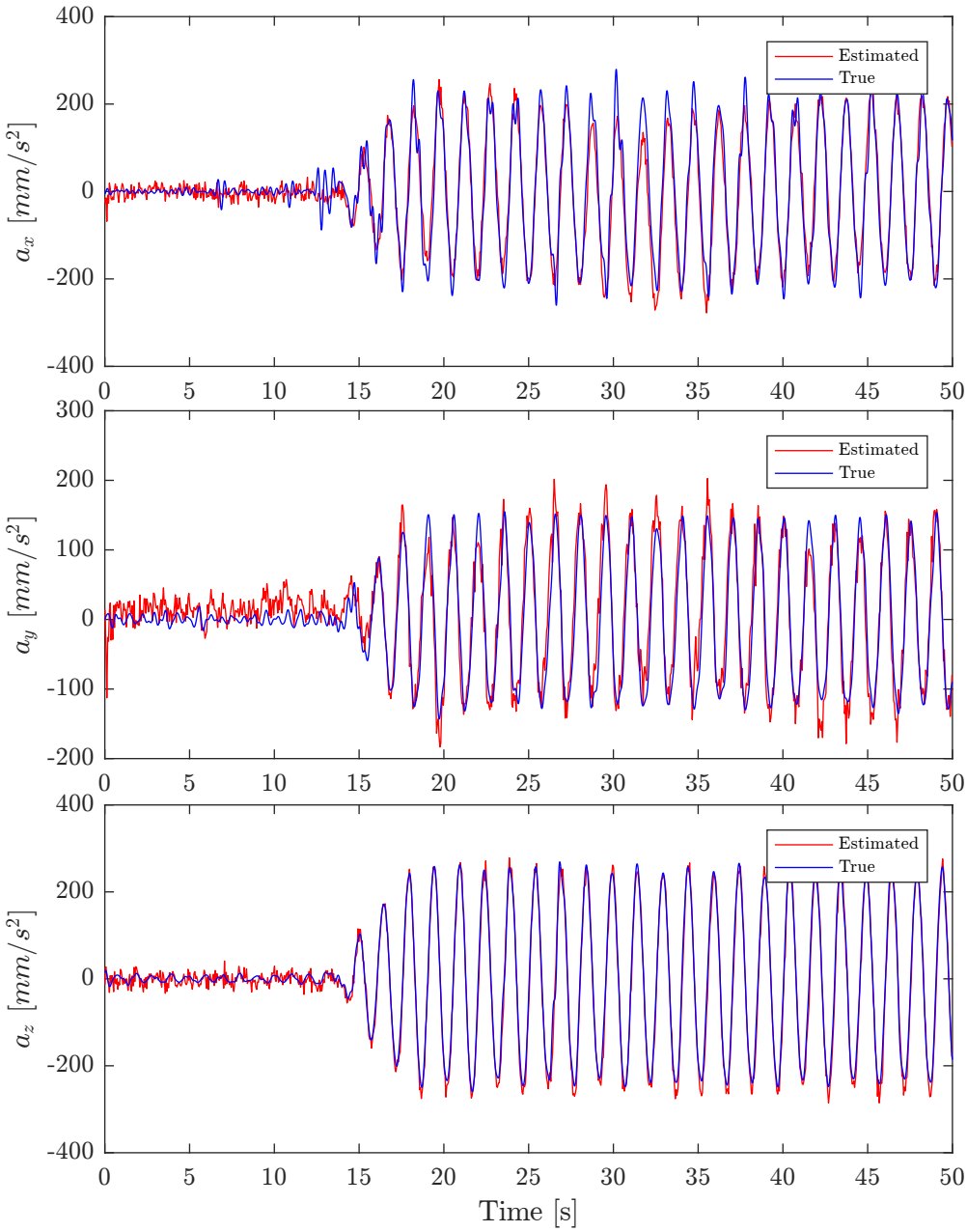

Figure 5.1: Estimated and true translational accelerations in CO with 30 degree heading. Upper figure show acceleration in surge, middle in sway and lower figure in heave.

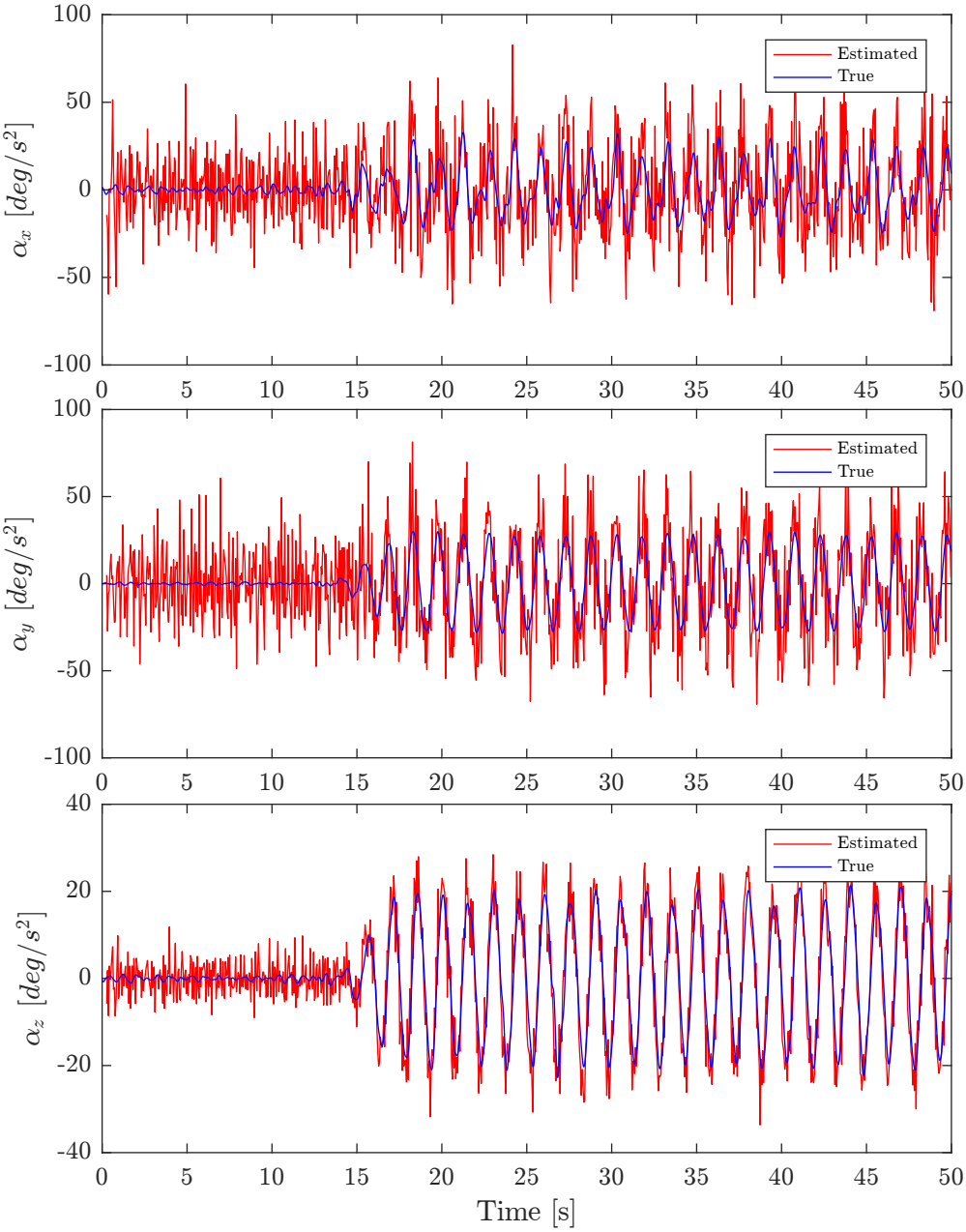

Figure 5.2: Rotational acceleration in CO with 30 deg heading. Upper figure show acceleration in roll, middle in pitch and lower in yaw.

5.3 Accelerations in SO

The same experiment is presented here as for accelerations in CO, using the method presented in Section 3.3. The process and measurement noise covariance matrices were set based on the actual variance with some manual adjustments. The true values presented are based on measurement from Qualisys, and calculated according to the method presented in Section 3.4. In Figure 5.3 the estimated and true linear acceleration in SO for IMU #1 and #2 are presented, while IMU #3 and #4 are presented in Figure 5.4. For all sensors, the estimated accelerations in surge indicate the same tendency of slowly oscillations as the estimates in CO. The estimated accelerations in sway show some trace of oscillatory overestimating the signal, especially for IMU #3 and #4. In heave, the method performs well with small deviations from true acceleration. However, the estimated value is continuously a little higher than the true. It should be noted that the accuracy of the true acceleration is affected by the measurement noise in the position of the sensors relative CO. The lever arm from SO to CO is input to the calculations, and thus the true acceleration has higher uncertainty.

5.4 Estimating direction of incoming waves from phase difference in roll, pitch and yaw

The phase difference between motions in roll, pitch and yaw are presented here. The result for heading fixed to 30 degrees is chosen to present in this section as an illustration of the phase difference between roll and pitch, see Figure 5.5. Each radius corresponds to the specified wave period in the radial ticks, and the polar angles represent the phase difference. As seen in Figure 5.5, the phase difference between roll and pitch is close to zero for wave periods longer than 1 second, while the phase difference is around -75 degrees for a wave period of 1 second.

Figure 5.6 presents the phase difference for all 4 headings evaluated, where each color represents one heading. For 30 and 60 degree heading the phase difference is very similar, while 120 and 150 degrees are in antiphase. Wave period of 1 second does

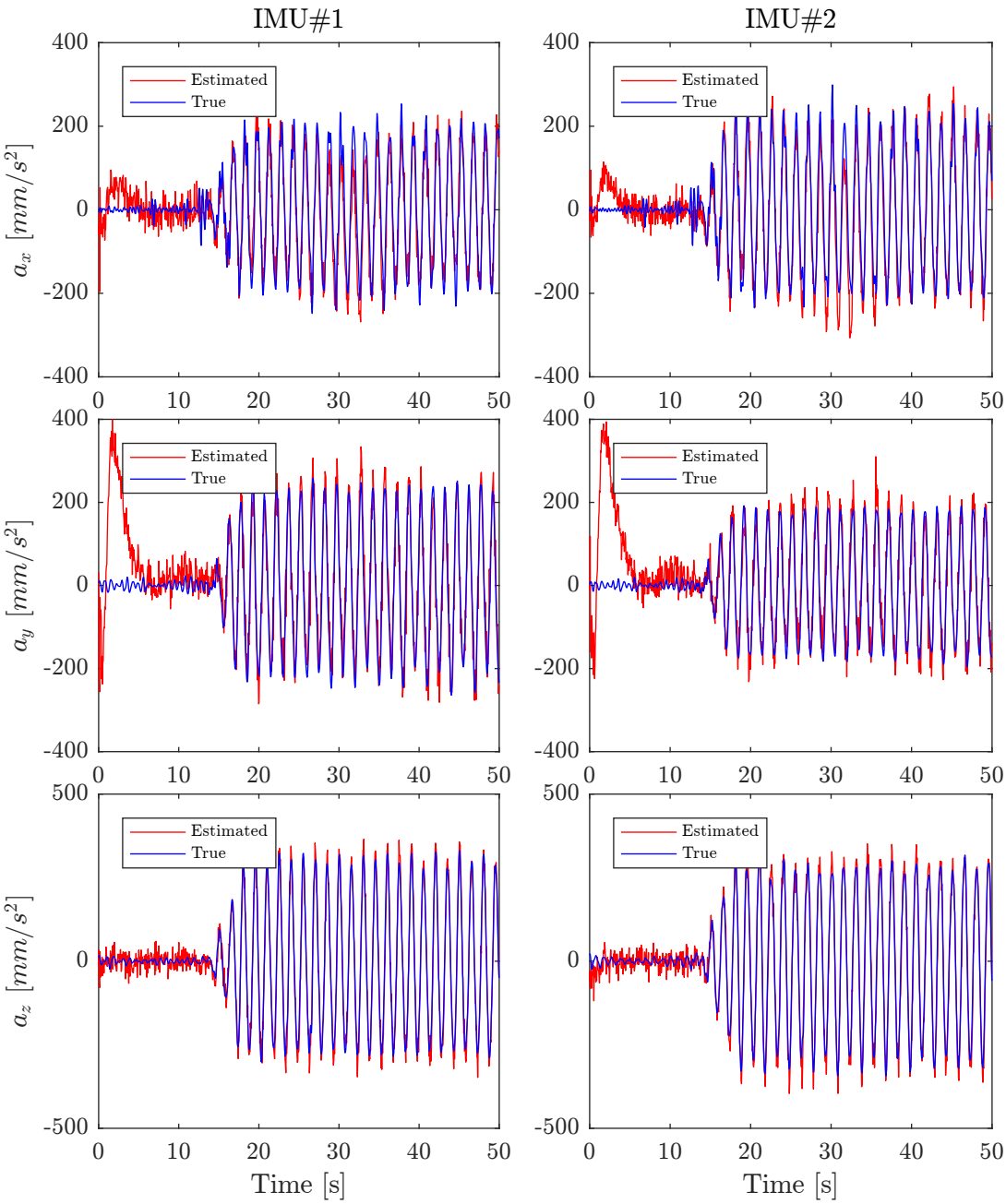

Figure 5.3: Estimated and true translational accelerations in SO for IMU #1 and #2. Left figures are accelerations in {s1}, right figures are in {s2}. Upper figures show surge, middle sway and lower heave.

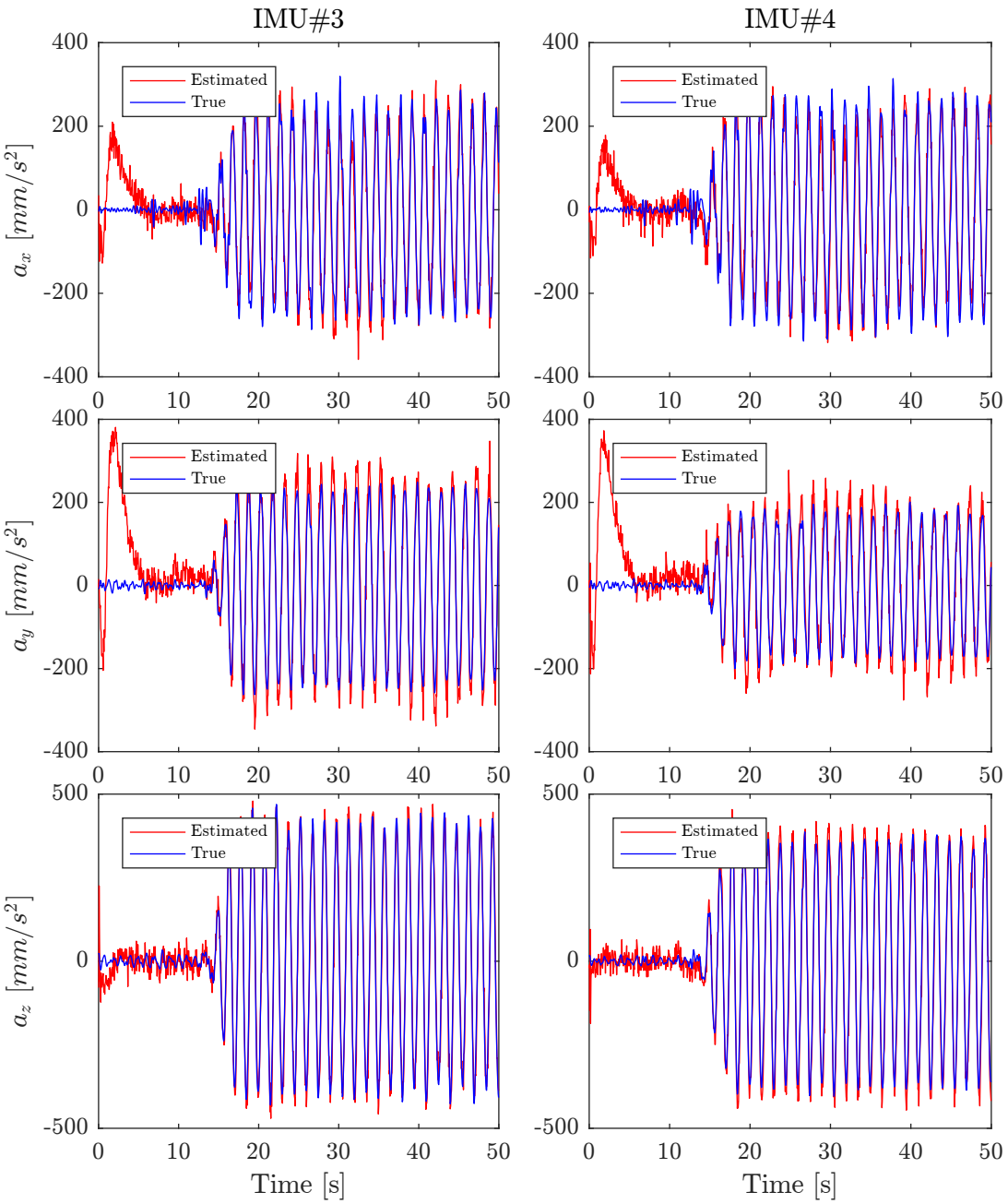

Figure 5.4: Estimated and true translational accelerations in SO for IMU #3 and #4. Left figures are accelerations in {s3}, right figures are in {s4}. Upper figures show surge, middle sway and lower heave.

not show the same similarity as longer periods. For headings of opposite sign, it is assumed that the phase difference will shift 180 degrees. For example, when considering headings of 30 and -30 degrees, if the phase difference in roll and pitch is positive for 30 degrees, then it will be negative for -30 degrees. Hence, a 180 degree shift is assumed for headings with opposite sign.

In Figure 5.7 the phase difference between roll and yaw is presented. As for roll and pitch, there are some correlation between 30 and 60 degrees, and similarly for 120 and 150 degrees. Also, wave period of 1 second stands out from the other periods. For headings with opposite sign it is assumed that the phase difference will be the same, as both roll and yaw will turn with the opposite signs.

Finally, the phase difference between pitch and yaw is presented in Figure 5.8. The figure show stronger correlation between all headings and wave periods, as almost all have a phase difference between -60 and -120 degrees. For opposite sign headings it is assumed that the phase difference will be shifted 180 degrees, as pitch has the same positive movement while yaw will change direction.

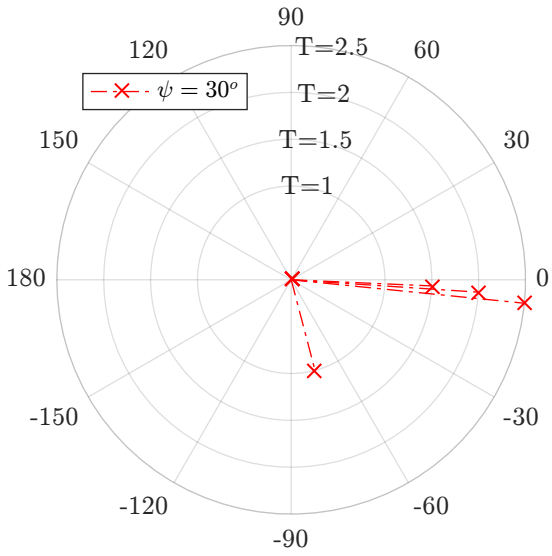

Figure 5.5: Illustrative phase difference plot between roll and pitch with heading 30 degrees. Each radius correspond to the specified wave period in model scale, and the polar angle represent the phase difference between roll and pitch.

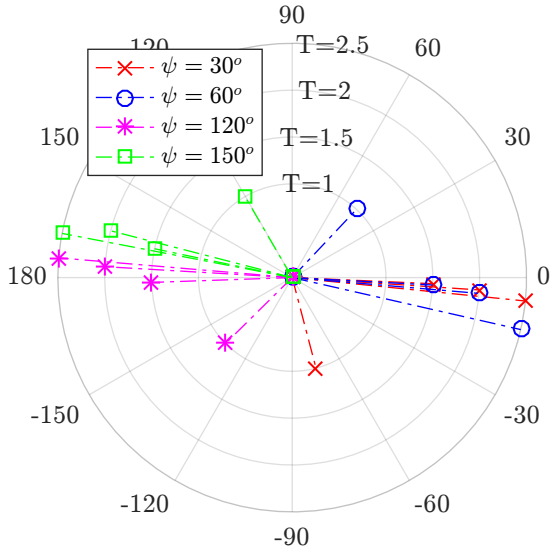

Figure 5.6: Phase difference in roll and pitch. Each radius corresponds to the specified wave period in model scale, and the polar radius represent the phase difference between roll and pitch. The different colors represent different headings of the vessel.

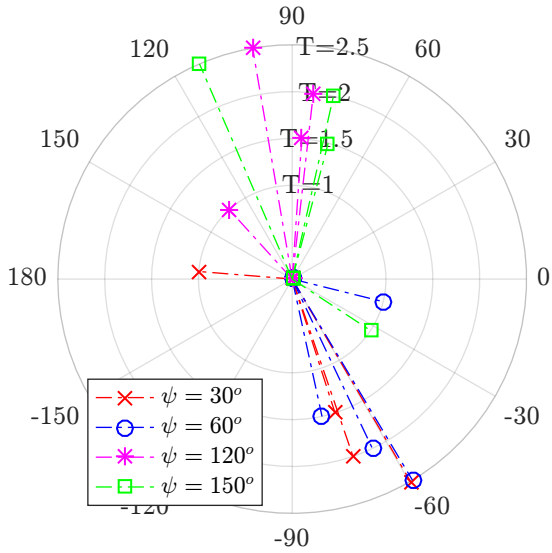

Figure 5.7: Phase difference between roll and yaw for all headings and periods.

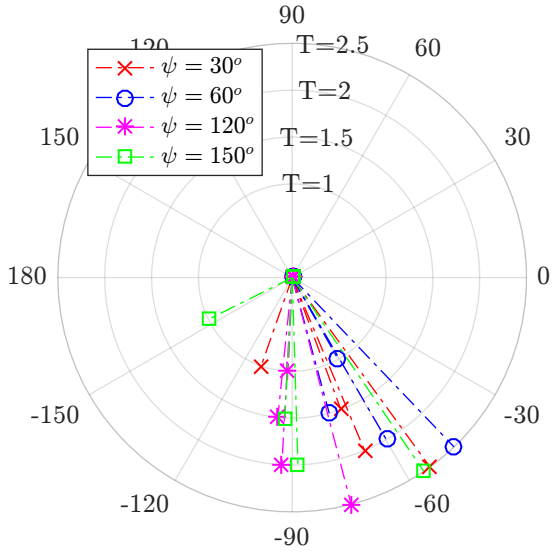

Figure 5.8: Phase difference between pitch and yaw for all headings and periods.

5.5 Estimating direction of incoming waves based on horizontal forces

The final proposed method to estimate the direction of incoming waves is based on the distributed horizontal accelerations in the hull. In Figure 5.9 the heading ψ of the vessel as it drifts of with the waves is given in the upper figure, while the three lower present accelerations estimated for all IMU's in surge, sway and heave, respectively. The vessel starts to oscillate in surge and heave when the wave hits the vessel, and after approximately 10 seconds sway acceleration is induces. What is noteworthy, is the strong difference in heave accelerations between starboard(IMU#2 and #3) and port(IMU#1 and #4). The vessel started to roll strongly with only a small offset in heading from head sea. This experiment is shown in the video of Udjus (2017).

To examine if it is possible to draw conclusion on the direction of incoming waves from the horizontal accelerations, the moving average over one period is presented for all IMU's in surge and sway in Figure 5.10. The heading of the vessel drifted towards

port, and thus the vessel will drift in negative x and y direction in {b}. However, as the moving average figure shows, it is hard to draw conclusion on which direction the vessel is drifting. Also, the accelerations in sway is very similar for all four IMU's and thus it is hard to conclude on the forces acting on the vessel. In Figure 5.11 the maximum and minimum sway accelerations for all IMU's are presented, with the objective of determining difference in magnitude for positive and negative accelerations. It is seen that positive accelerations in sway have a higher magnitude than negative. However, towards the end of the experiment, the difference between them diminishes. It is assumed that the reason for these results comes from the slowly oscillating effect seen in the accelerations estimated SO, as discussed in Section 5.3.

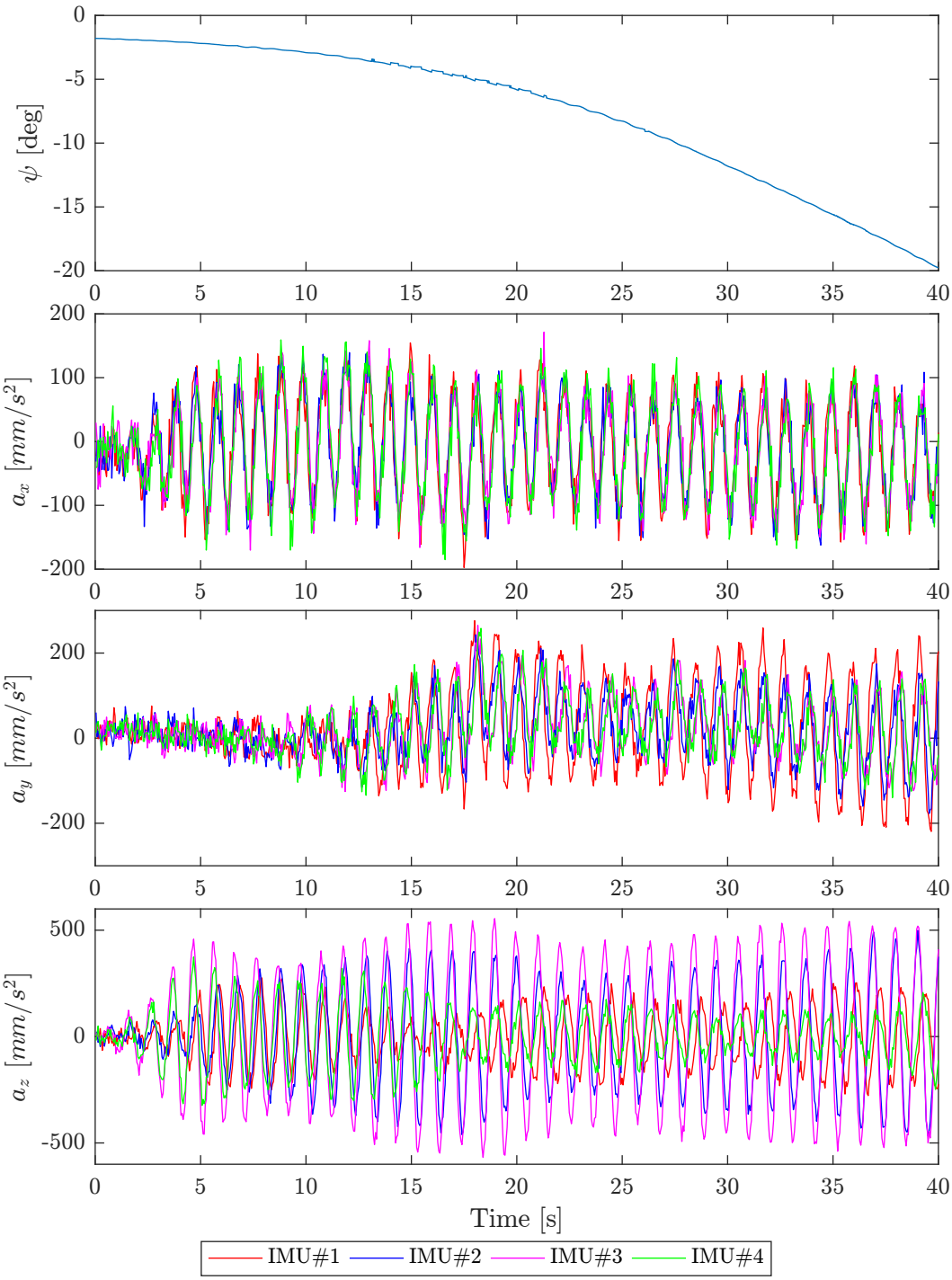

Figure 5.9: Local accelerations in free floating, with wave period T=1s. Upper figure shows heading of vessel expressed in {f}. The lower three show estimated accelerations in surge, sway and heave, respectively, for all sensors.

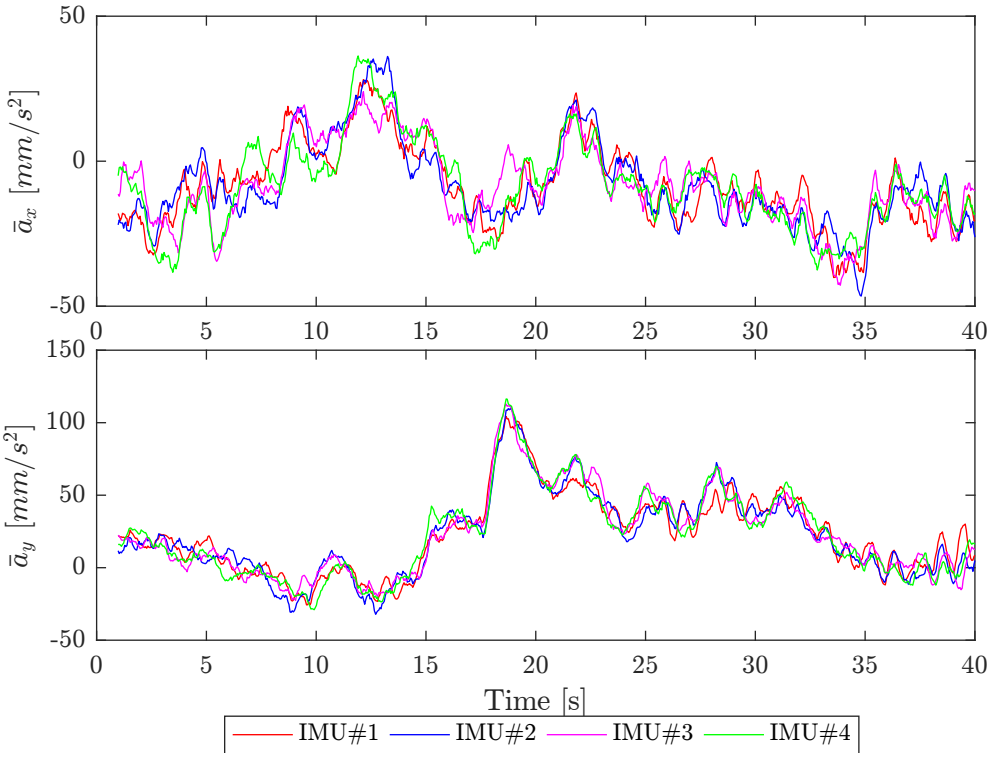

Figure 5.10: Moving average in surge and sway in free floating, for all IMU's. The moving average period is over 1s. Upper figure shows acceleration in surge, and lower figure in sway.

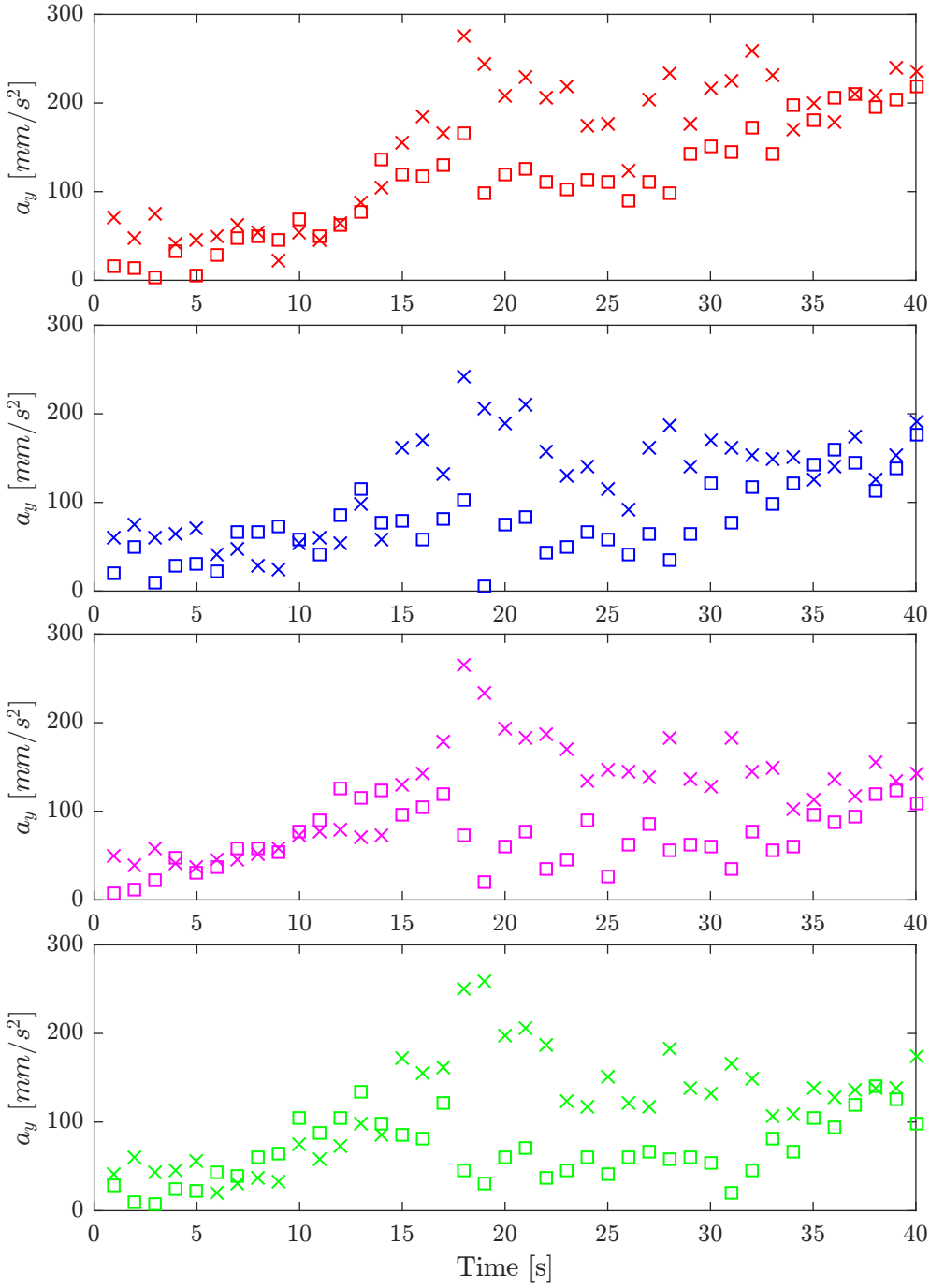

Figure 5.11: Maximum and minimum acceleration in sway for all IMU's during free floating experiment. Crosses are maximum accelerations, and squares are absolute value of minimum accelerations. IMU#1 to #4 from top to bottom.

5.6 Estimating direction of incoming waves from time difference in heave accelerations

The results presented here are based on the method for estimating the direction of incoming waves as described in Section 3.5.3. The time series presented starts when the wave train hits the vessel, and stops before the reflected waves from the end of the basin returns. The angle of incoming waves, β, is modeled with steps of 10 degrees to find the direction with minimum time difference. The estimated angles have some variance, and they are assumed to be Gaussian distributed when calculating the standard deviation.

In Figure 5.12 the time series of estimated direction of incoming waves is plotted for head sea and wave period of 1.5 seconds. The mean value of the estimated angles is annotated in the figure, together with the standard deviation. The estimates have a large variance, while the mean value is close to the true direction. Similarly, Figure 5.13 shows the estimated direction for head sea and wave period of 2 seconds. The method performs better in terms of mean value, while the variance is higher for this period.

The mean estimate and standard deviation for all headings and wave period of 1.5 and 2 seconds are presented in Figure 5.14 and 5.15, respectively. The polar plots illustrate estimated direction of incoming waves expressed in {b}. For wave period of 1.5 seconds, the method performs well for all headings with a maximum discrepancy of 12 degrees. The standard deviation varies some, where head and beam sea have larger variance compared to headings between 30 and 120 degrees. With wave period of 2 seconds the performance is poorer, and for some headings the method is not able to estimate the correct direction of incoming waves. This is especially clear for heading equal 120 degrees, where the error in mean estimated direction is 54 degrees and the standard deviation is 109 degrees. Compared to wave period of 1.5 seconds, the standard deviation is much larger for all headings.

In order to look into the difference in performance for each wave period, a short

time series when the wave hits the vessel is presented. Figure 5.16 shows the heave acceleration of all IMU's with zero degrees heading and wave period of 1.5 seconds, and Figure 5.17 with 120 degrees heading and waves of 2 seconds. The local maximum and minimum values for all sensors are marked. In both figures it is clear that the located maximum and minimum accelerations are affected by noise. For longer wave periods the oscillating acceleration will be less step, and thus the noise gets higher influence on the timing of the local extrema. In addition, it can be seen that the method does not perfectly locate the extrema values, as the minimum value for IMU#1 around 8 seconds is not in fact the minimum value.

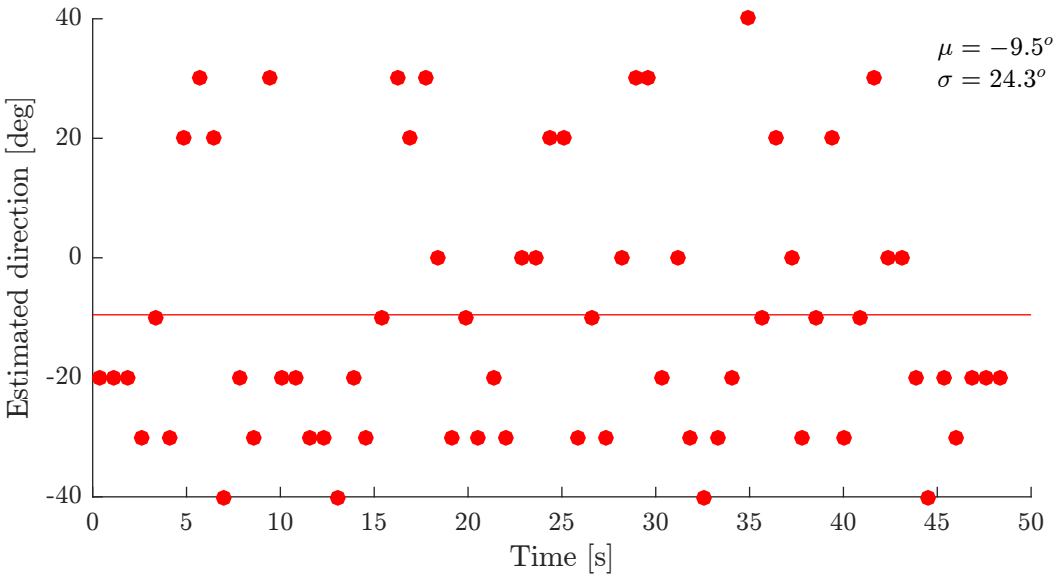

Figure 5.12: Time series of estimated direction of incoming wave with heading fixed to zero degrees and T=1.5s. The line is the mean value of the estimated angels, and the standard deviation is annotated in the Figure.

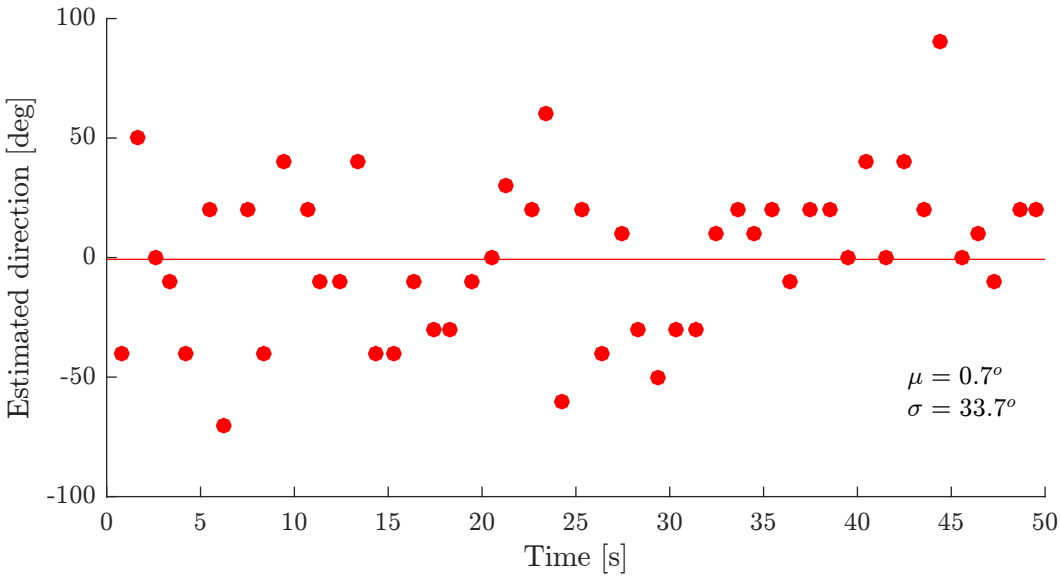

Figure 5.13: Time series of estimated direction of incoming wave with heading fixed to zero degrees and T=2s. The line is the mean value of the estimated angels, and the standard deviation is annotated in the Figure.

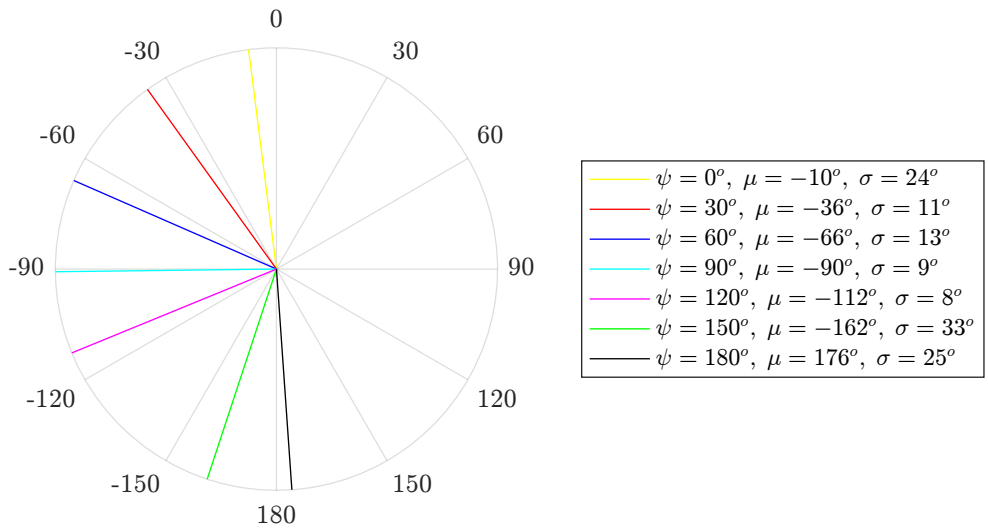

Figure 5.14: Estimated angles of incoming waves for all headings with T=1.5s.

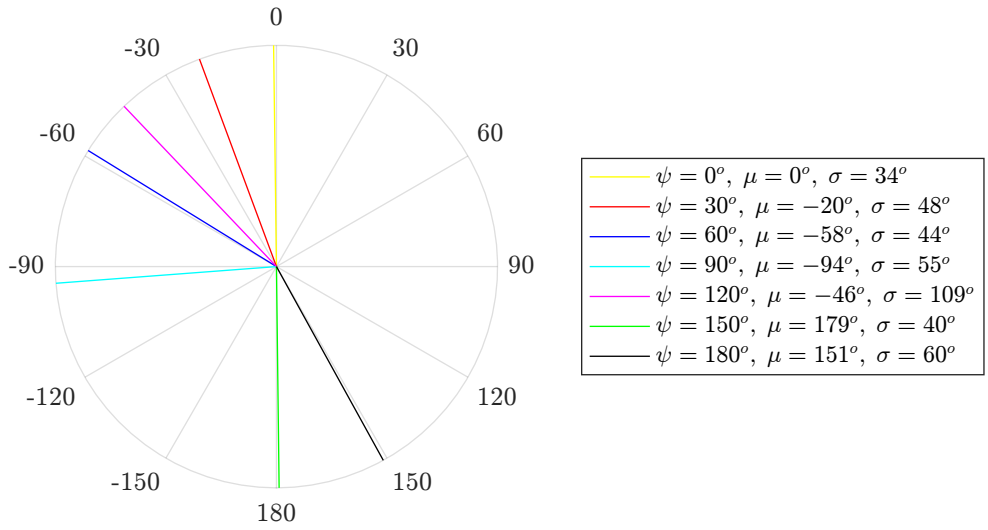

Figure 5.15: Estimated angles of incoming waves for all headings with T=2s. Each color represent one different heading as given in the legend. The mean value of estimated angle is also given in the legend, together with standard deviation of the estimates. The polar angles represent the estimated direction of incoming waves, expressed in {b}

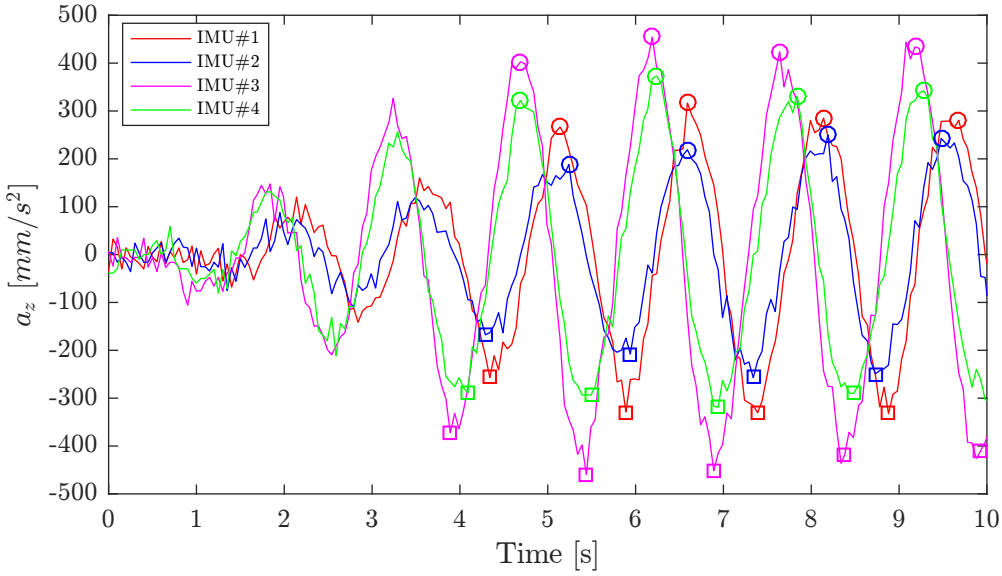

Figure 5.16: Acceleration in heave for all IMU's when wave train approach the vessel. Heading fixed to zero degrees and T=1.5s. Circles and squares mark local maximum and minimum as input for estimating direction of incoming waves.

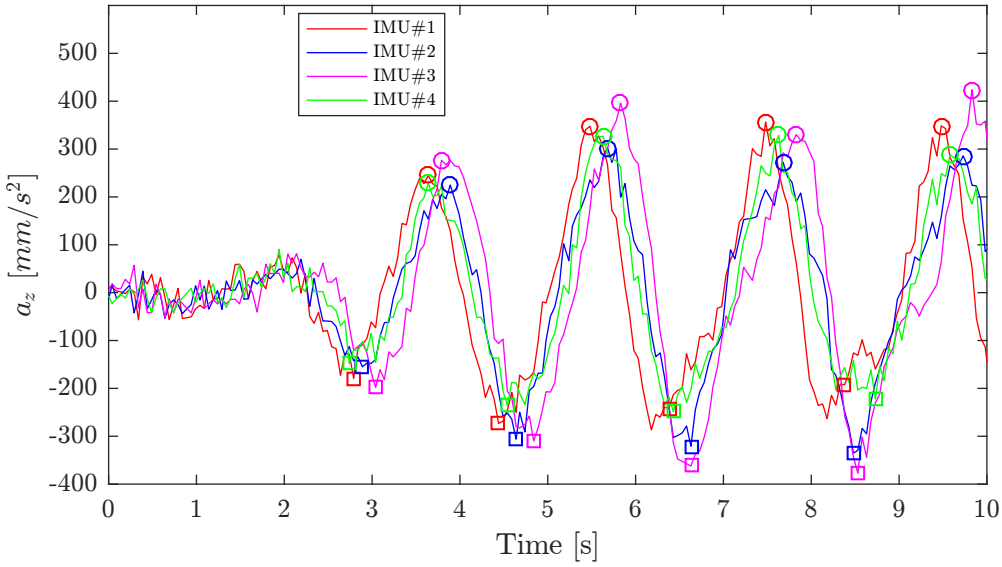

Figure 5.17: Acceleration in heave for all IMU's when wave train approach the vessel. Heading fixed to 120 degrees and T=2s. Circles and squares mark local maximum and minimum as input for estimating direction of incoming waves.

5.7 Spatial variability and probability fit of heave accelerations

To explore the spatial variability of accelerations, sensor configuration 2 was chosen as this one has the largest spatial range between the sensors. In Figure 5.18 the PSD using Welch' method is shown for heave acceleration with head sea and wave period of 2 seconds. As can be seen, the power of the signal is centered around a frequency of 0.5 Hz, i.e. the wave frequency. Further, the figure show that the power varies for the different IMU's, where IMU#4 has most energy and IMU#1 has least. For the same waves, but heading set to 180 degrees, Figure 5.19 show that IMU#2 and #4 now have the same power.

The heave accelerations for all IMU's in both headings are presented in probability distribution plots in Figure 5.20 and 5.21. As expected, the heave accelerations show strong similarities to normal distribution. This is illustrated in Figure 5.22, where the cumulative distribution of IMU#4 with heading 180 degrees is shown together with a normal distribution fit of the data. The probability distribution figures also illustrate how the magnitude of heave accelerations are higher in IMU#2 when the vessel is exposed to following sea.

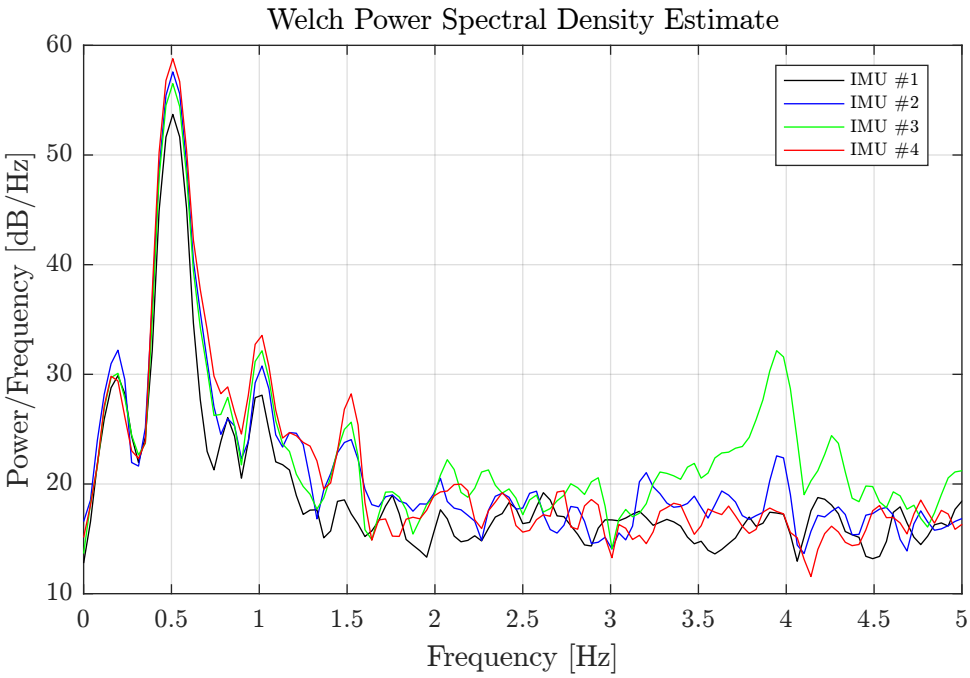

Figure 5.18: Welch PSD plot for all IMU's in sensor configuration 2. Heading fixed to 0 degrees and T=2s.

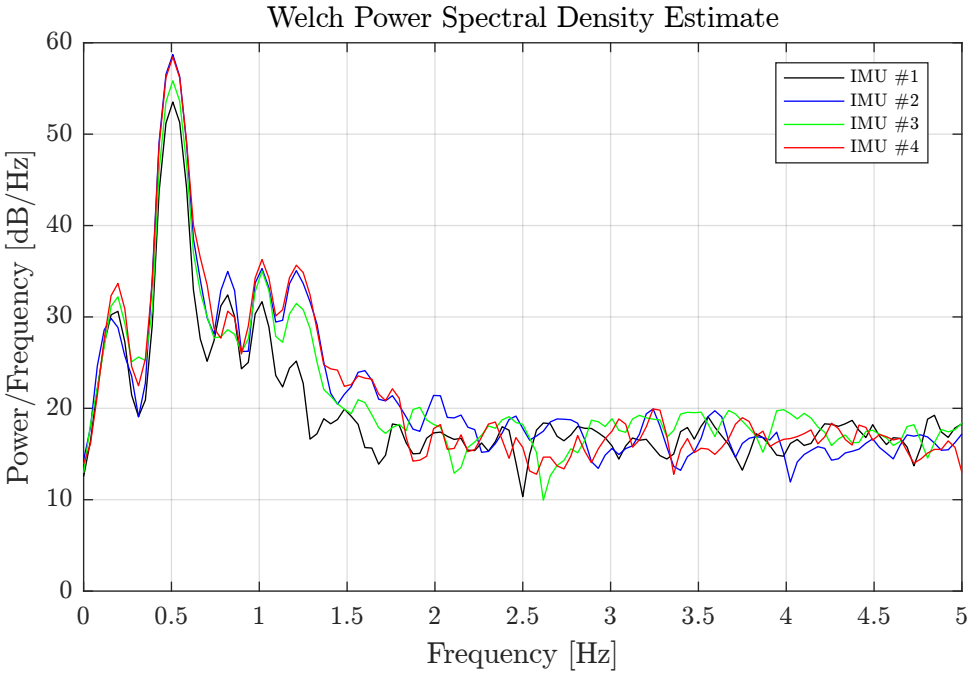

Figure 5.19: Welch PSD plot for all IMU's in sensor configuration 2. Heading fixed to 180 degrees and T=2s.

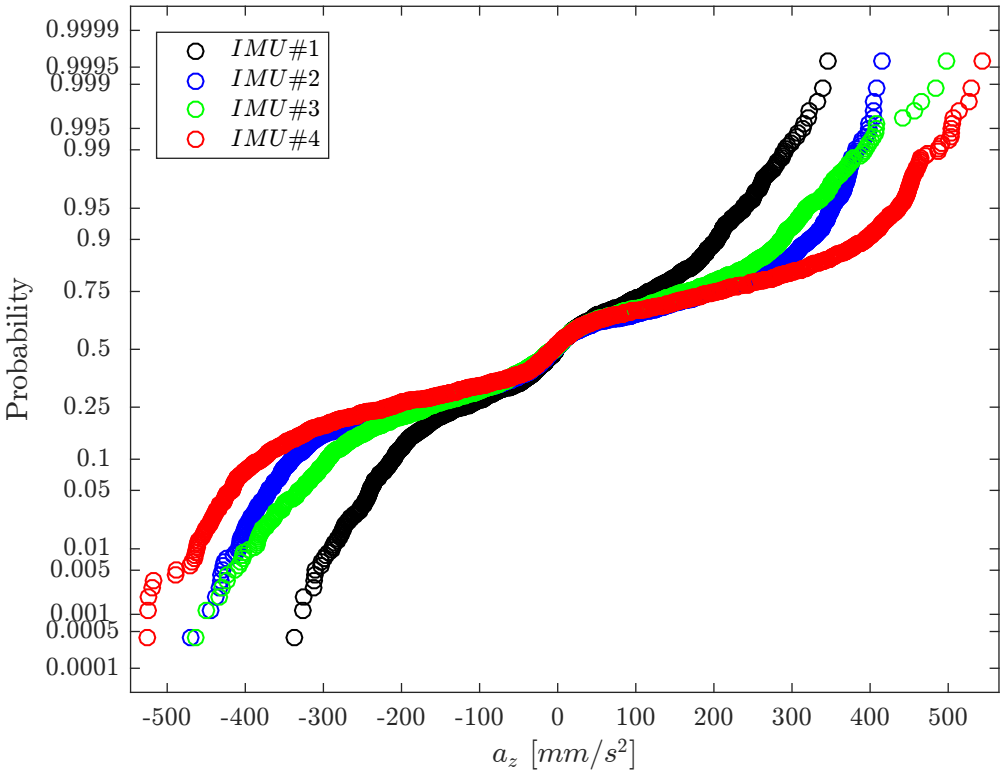

Figure 5.20: Probability Distribution for all IMUs in sensor configuration 2. Heading fixed to 0 degrees and T=2s.

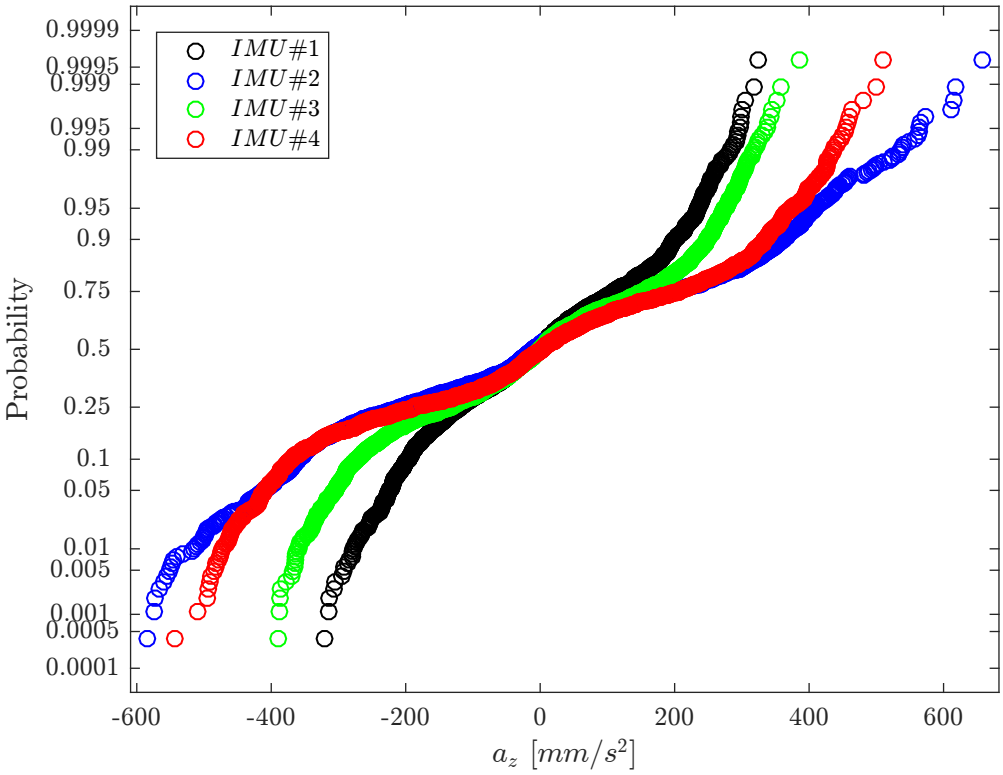

Figure 5.21: Probability Distribution for all IMUs in sensor configuration 2. Heading fixed to 180 degrees and T=2s.

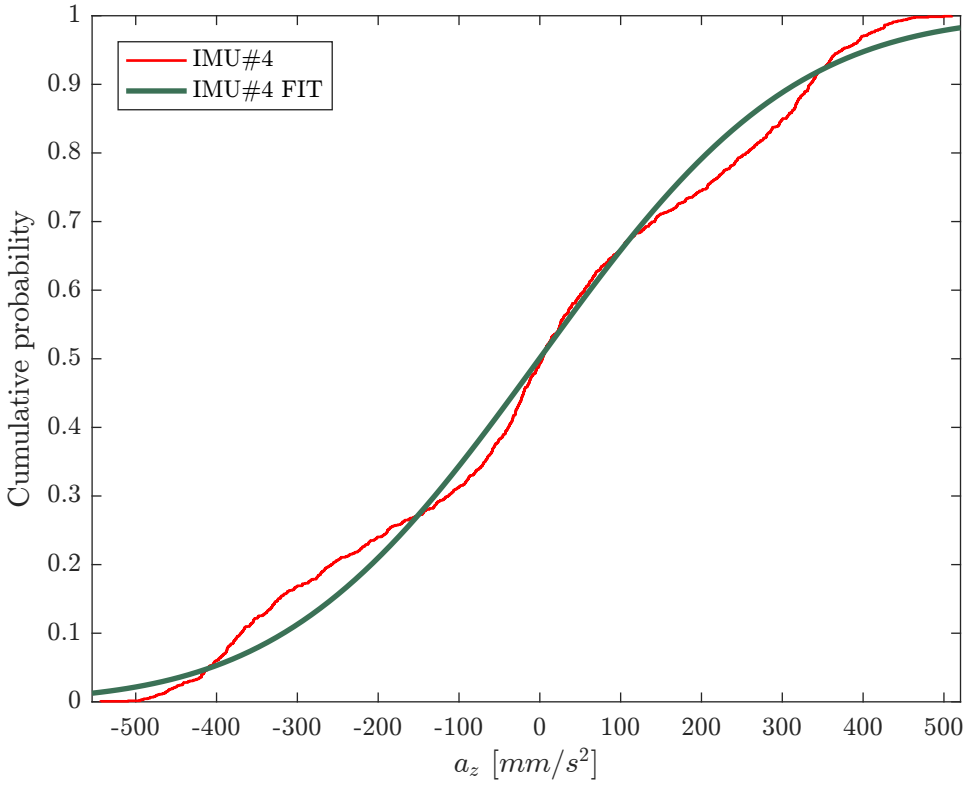

Figure 5.22: Cumulative distribution and normal distribution fit for heave acceleration in IMU#4. Heading fixed to 180 degrees and T=2s.

Chapter 6

Results

The system of spatially distributed inertial measurement units performed well for as a virtual 6 DOF sensor in CO. The linear accelerations in surge, sway and heave are best, with small discrepancies from the true accelerations. Rotational accelerations in roll, pitch and yaw are more influenced by noise, but is still able to estimate the tendency of the motion. The results show that estimation of yaw acceleration has best performance.

The method for estimating linear accelerations in each SO is also found to perform well, compared to the calculated true values. The main objective of this method is to filter out gravity and bias, which is achieved. As for estimation in CO, the heave estimate is the best for all sensors in SO, but still show a small tendency to overestimate. Surge and sway estimates have some slowly oscillating effects for all sensors, but still the filter performance is quite good. Also, the true acceleration calculated in SO is affected by the measurement error in the position of each sensor origin relative CO, and thus the true values in SO have less accuracy than the true accelerations in CO.

Estimating direction of incoming waves based on correlation between motion in roll, pitch and yaw gave some results. For wave periods longer than 1 second, phase difference between roll-pitch and roll-yaw showed strong correlation for headings $0-90^o$ and $90-180^o$. As for pitch and yaw motion, there was not much difference between the different headings. The results show it is hard to distinguish between e.g.

direction of 30 and 60 degrees, but still some estimates can be made. Table 6.1 gives a summary of how the direction of incoming waves can be estimated based on the phase difference between the different rotational motions. Each cell in the table represent the interval of β, i.e. the angle where waves are coming from expressed in {b}.

Table 6.1: Direction of incoming waves from phase difference in roll, pitch and yaw

		Roll-Pitch	
		$\approx 0^o$	$\approx 180^o$
Roll-Yaw	$\approx 90^o$	$< 90^o, 180^o >$	$< -90^o, -180^o >$
	$\approx -90^o$	$< 0^o, -90^o >$	$< 0^o, 90^o >$

Estimating direction of incoming waves from analysis of spatially distributed accelerations in surge and sway was less successful. This method requires very accurate estimates of the accelerations, and due to the small errors seen in surge and sway, it was not possible to provide useful information on the force field in the horizontal plane. The moving average acceleration in sway was most of the time positive, which would mean that the vessel drifts towards the waves. However, it should be noted that only one experiment was performed when the heading of the vessel drifts, and thus the method might still be useful for other wave periods and headings.

Using the spatially distributed heave accelerations over time as the waves travel through the vessel gave variable results. With wave period of 1.5 seconds, the method performed well, and was able to estimate the direction with an error in the mean value less than 15 degrees. However, the estimates had a significant variance, and should thus only be used in combination with a moving average, for example. For longer periods, and thus faster waves, the performance was poorer. At some heading the method was not able to estimate the direction at all, and the variance of the estimates were significantly higher.

Finally, PSD analysis of heave acceleration for sensor configuration 2 showed that heave acceleration varies within the hull. It was also found that following sea in-

duced much higher accelerations in the aft than head sea. The probability plot also showed that the heave accelerations have strong similarities to normal distribution, as expected for the actual wave spectrum.

Chapter 7

Conclusion

The embedded systems of IMU's connected to microcontrollers communicating over a network proved to be an efficient system for measuring spatially distributed accelerations in the hull. It provides time-synchronized and accurate measurements for motion estimation and force field identification.

Four non-planar spatially distributed sensors worked well as a virtual 6 DOF accelerometer in CO, with best results for surge, sway, heave and yaw accelerations while roll and pitch were more noisy. Estimating translational accelerations in each SO was also successful, with a high accuracy. Hence, the system provides a method for measuring the local forces, which can be used to identify the surrounding force field. By investigating local heave accelerations, one could clearly see the wave forces traveling through the hull.

The three proposed methods for estimating direction of incoming waves had variable results. There were some correlation between motion in roll, pitch and yaw which can give rough estimates of the direction of incoming waves. Local accelerations in surge and sway did not provide sufficient information to conclude on the surrounding force field, as they were highly affected by roll motion. Time-difference in heave acceleration between the sensors gave good estimates of direction of incoming waves in some wave periods, and can be used as a method for weather vaning the vessel.

Chapter 8

Further work

There are several topics that are interesting to further explore. One disadvantage with the experimental setup, is that the straps constrained the vessel from motion in several DOFs. Analysis of local accelerations in surge and sway with the vessel freely floating for different headings would be interesting, in order to see if the force field can be identified in this way.

The method for estimating direction of incoming waves based on time difference in heave accelerations might also perform better for a different sensor configuration. By mounting the sensors with a higher span in the horizontal plan, the performance might improve. For example, placing the the aft sensors with equal distance in x-direction from CO would be interesting.

It was also found that the computational power of the cRIO was limited, and the high number of variables introduced with all IMU's caused some problems. One possibility might be to utilize the processors in each microcontroller, for example by implementing the algorithm for estimation of translational accelerations in SO in each microcontroller. Doing this would require the cRIO to send the vessel position to each sensor, but the upside is less computations for the cRIO.

It would be interesting to use the estimated direction of incoming waves as input to a heading controller for weather vaning in DP-operations, and compare the performance to standard weather vaning methods. As described in Fossen (2011), standard

methods for weather optimal heading control of a vessel are based on minimizing energy consumption or reducing thrust in sway. These methods are not based on measurements of environmental forces, but rather optimization of the current situation, and thus take some time. Hence, as an alternative to these methods, the following control objective is suggested for weather optimal heading based on the estimated direction of incoming waves:

$$\lim_{t\to\infty} [\psi(t) - \psi_d(t)] = 0 \tag{8.1}$$

where $\psi_d(t) = \psi(t) + \beta$. To achieve this objective, the desired angle should be used as input to an autopilot model, for example the Nomoto model as described in Nomoto et al. (1957).

Bibliography

Analog Devices, 2017. Data Sheet ADIS16364, 5th Edition.
URL http://www.analog.com/media/en/technical-documentation/data-sheets/ADIS16364.pdf

Arduino, 2017. Arduino LEONARDO ETH.
URL http://www.arduino.org/products/boards/arduino-leonardo-eth

Balchen, J. G., Jenssen, N. A., Sælid, S., 1976. Dynamic positioning using kalman filtering and optimal control theory. In: IFAC/IFIP symposium on automation in offshore oil field operation. Vol. 183. p. 186.

Batista, P., Silvestre, C., Oliveira, P., 2011a. On the observability of linear motion quantities in navigation systems. Systems & Control Letters 60 (2), 101–110.

Batista, P., Silvestre, C., Oliveira, P., Cardeira, B., 2011b. Accelerometer calibration and dynamic bias and gravity estimation: Analysis, design, and experimental evaluation. IEEE transactions on control systems technology 19 (5), 1128–1137.

Bjørnø, J., 2016. Thruster-assisted position mooring of c/s inocean cat i drillship. Master's thesis, Norwegian University of Science and Technolog.

Breivik, M., 2010. Topics in guided motion control of marine vehicles. Thesis, Norwegian University of Science and Technology, Faculty of Information Technology, Mathematics and Electrical Engineering, Department of Engineering Cybernetics.

Chambers, L., Akanyeti, O., Venturelli, R., Ježov, J., Brown, J., Kruusmaa, M., Fiorini, P., Megill, W., 2014. A fish perspective: detecting flow features while moving using an artificial lateral line in steady and unsteady flow. Journal of The Royal Society Interface 11 (99), 20140467.

Fall, K. R., Stevens, W. R., 2011. TCP/IP illustrated, volume 1: The protocols. addison-Wesley.

Faltinsen, O., 1993. Sea loads on ships and offshore structures. Vol. 1. Cambridge university press.

Fossen, T., Perez, T., 2004. Marine systems simulator (mss).
URL http://www.marinecontrol.org

Fossen, T. I., 2000. A survey on nonlinear ship control: from theory to practice. IFAC Proceedings Volumes 33 (21), 1 – 16, 5th IFAC Conference on Manoeuvring and Control of Marine Craft (MCMC 2000), Aalborg, Denmark, 23-25 August 2000.

Fossen, T. I., 2011. Handbook of marine craft hydrodynamics and motion control. John Wiley & Sons.

Gleason, A., 2013. Interfacing adis16364 with arduino.
URL https://github.com/agleason6/ADIS16364_example

Gurgel, K.-W., Essen, H.-H., 2000. On the performance of a shipborne current mapping hf radar. IEEE journal of oceanic engineering 25 (1), 183–191.

Handbook, M.-L., 2016. Marine cybernetics laboratory handbook.
URL https://github.com/NTNU-MCS/MC_Lab_Handbook

Janabi-Sharifi, F., Hayward, V., Chen, C.-S., 2000. Discrete-time adaptive windowing for velocity estimation. IEEE Transactions on control systems technology 8 (6), 1003–1009.

Kalman, R. E., 1960. A new approach to linear filtering and prediction problems. Journal of basic Engineering 82 (1), 35–45.

Kjerstad, Ø. K., Skjetne, R., 2016. Disturbance rejection by acceleration feedforward for marine surface vessels. IEEE Access 4, 2656–2669.

Kongsberg Maritime, 2017. Autonomous ship project, key facts about YARA Birkeland. URL https://www.km.kongsberg.com/ks/web/nokbg0240.nsf/AllWeb/4B8113B707A50A4FC125811D00407045?OpenDocument

Leira, B., Børsheim, L., Espeland, Ø., Amdahl, J., 2009. Ice-load estimation for a ship hull based on continuous response monitoring. Proceedings of the Institution of Mechanical Engineers, Part M: Journal of Engineering for the Maritime Environment 223 (4), 529–540.

Mathworks, 2017a. Signal Processing Toolbox User's Guide (R2017a). URL https://se.mathworks.com/help/pdf_doc/signal/signal_tb.pdf

Mathworks, 2017b. Take Derivatives of a Signal(R2017a). URL https://se.mathworks.com/help/signal/ug/take-derivatives-of-a-signal.html?s_tid=gn_loc_drop

Nomoto, K., Taguchi, T., Honda, K., Hirano, S., 1957. On the steering qualities of ships. Tech. Rep. Vol. 4, International Shipbuilding Progress.

Parks, T., McClellan, J., March 1972. Chebyshev approximation for nonrecursive digital filters with linear phase. IEEE Transactions on Circuit Theory 19 (2), 189–194.

Pettersen, B., 2007. Marin teknikk 3: Hydrodynamikk. Dept. of Marin Techn. NTNU, Trondheim, Norway.

Qualisys, 2011. Qualisys Track Manager User Manual. URL http://fy.chalmers.se/~f7xiz/TIF081C/QTM-usermanual.pdf

Skjetne, R., 2005. The maneuvering problem. Ph.D. thesis, Norwegian University of Science and Technology, Faculty of Information Technology, Mathematics, and Electrical Engineering, Department of Engineering Cybernetics, Trondheim.

Smith, J. M., 1977. Mathematical modeling and digital simulation for engineers and scientists. Wiley, New York.

Soerensen, A. J., 2013. Marine control systems : propulsion and motion control of ships and ocean structures. Vol. UK-2013-76 of Kompendium (Norges teknisk-naturvitenskapelige universitet. Institutt for marin teknikk). Department of Marine Technology. Norwegian University of Science and Technology, Trondheim.

Tannuri, E. A., Sparano, J. V., Simos, A. N., Da Cruz, J. J., 2003. Estimating directional wave spectrum based on stationary ship motion measurements. Applied Ocean Research 25 (5), 243–261.

Udjus, G., 2017. Master's Thesis Presentation Video.
URL `https://vimeo.com/222068786`

Waals, O. J., Aalbers, A. B., Pinkster, J. A., 2002. Maximum likelihood method as a means to estimate the directional wave spectrum and the mean wave drift force on a dynamically positioned vessel.

Wang, W., Zhang, X., Zhao, J., Xie, G., 2015. Sensing the neighboring robot by the artificial lateral line of a bio-inspired robotic fish. In: Intelligent Robots and Systems (IROS), 2015 IEEE/RSJ International Conference on. IEEE, pp. 1565–1570.

Won, S.-h. P., Melek, W. W., Golnaraghi, F., 2010. A kalman/particle filter-based position and orientation estimation method using a position sensor/inertial measurement unit hybrid system. IEEE Transactions on Industrial Electronics 57 (5), 1787–1798.

Zappa, B., Legnani, G., Van Den Bogert, A. J., Adamini, R., 2001. On the number and placement of accelerometers for angular velocity and acceleration determination. TRANSACTIONS-AMERICAN SOCIETY OF MECHANICAL ENGINEERS JOURNAL OF DYNAMIC SYSTEMS MEASUREMENT AND CONTROL 123 (3), 552–553.

Appendix A

Embedded sensor system

A.1 Manual for using the system

All changes are made on the Arduino, and the IMU works as it is. In order to do changes on the Arduino code, it is advised to use the Arduino IDE which provides an easy way of building and uploading the code to the microprocessor. The Arduino code and necessary libraries are uploaded in the digital attachment to this thesis, in one folder for each sensor. On the lid of each sensor box, the IP-address and port that the Arduino sends the data packet is written, but can be easily be modified in the code.

Sampling rate is set by the Master sensor, and defines the frequency of interrupt signals. It was found that sampling and sending takes approximately 8ms, and thus it is assumed that 100Hz might be feasible. However, due to computational limitations on the cRIO, the sampling rate is set to 20Hz. Note that it is only the Master Arduino that sets the sampling rate, and this works as time-synchronization between the sensors.

There are three wires coming out of each sensor box, namely an IP-cable, power supply cables and the interrupt signal wire. The IP-cable should be connected to a network switch, on the same network as the recipient of the data(e.g. cRIO Ethernet port 2). The power supply should be connected to a 12V DC power grid, with blue wire connected to negative and red wire to positive. Finally, the white wire is the interrupt

signal, and the interrupt cable from the Master must be connected to the white wires from the slaves.

The Arduinos are programmed to send the IMU data as UDP packets of integers. To avoid loss of data, the measurements from the IMU are scaled with a factor of 1000, and casted to long integers before they are sent. The data string sent from the IMU consist of all data from the burst read command, i.e. voltage, tri-axis rotations, accelerations and temperatures, in addition to auxiliary voltage. In total 11 variables.

For the experiments in this thesis, the data packets were received on the cRIO. In order to receive the packets, a "custom device" code was programmed that scales the integers down to the correct float number, and split the string into desirable variables. Thus, the "IMU" custom device must be added in the VeriStand project file. The outputs from the custom device are voltage, translational accelerations and rotational velocities for all 4 IMU's, in total 28 variables. These can then be mapped as input to any Simulink code as desired.

A.2 Wiring IMU to microprocessor

The wiring between the breakout board for the IMU and the Arduino Leonardo ETH microprocessor are illustrated in Figure A.1. The breakout board part is named ADIS16IMU1/PCB, while the block named Digital I/O are the digital pins on the Arduino. The SPI bus on the Leonardo is named ICSP, and is in contradiction to most Arduinos not part of the standard digital pins but instead located in a group on one side of the board.

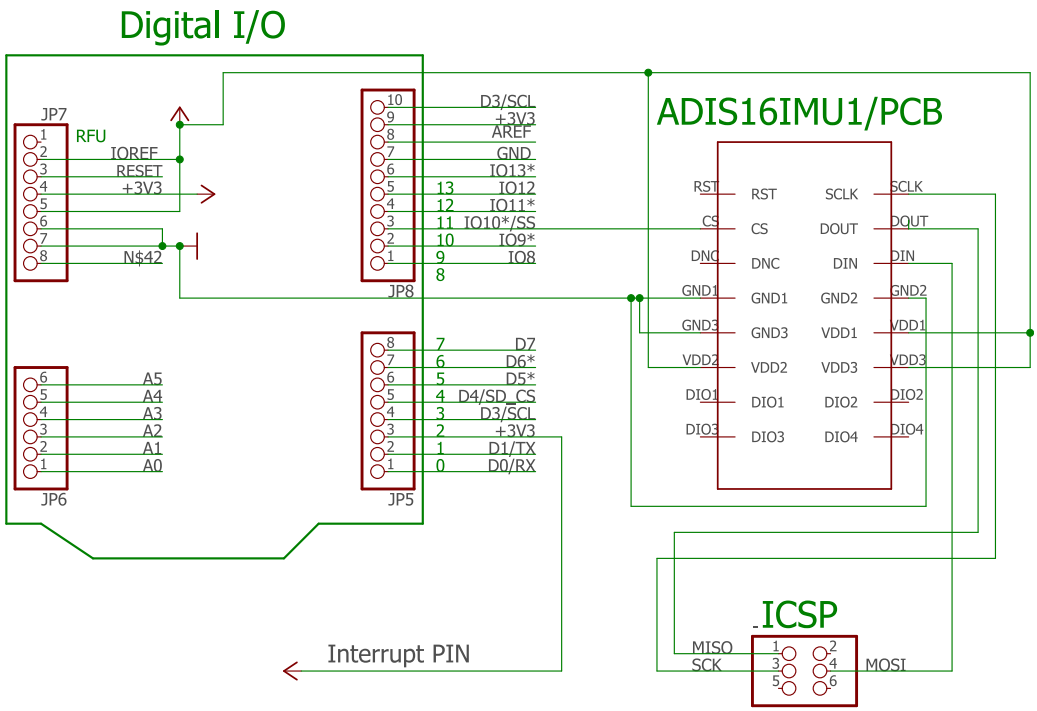

Figure A.1: Wiring diagram between Arduino and IMU breakout board